

This is a non-peer reviewed preprint submitted to EarthArXiv

# Ground Motion Characteristics of Subshear and Supershear Ruptures in the Presence of Sediment Layers

Mohamed Abdelmeguid<sup>1</sup>, Ahmed Elbanna<sup>2,3</sup>, Ares Rosakis<sup>1</sup>

<sup>1</sup>*Graduate Aerospace Laboratories, California Institute of Technology, Pasadena, CA 91125, USA.*

<sup>2</sup>*Department of Civil and Environmental Engineering, University of Illinois, Urbana-Champaign, IL 61801, USA*

<sup>3</sup>*Beckman Institute of Advanced Science and Technology, University of Illinois, Urbana-Champaign, IL 61801, USA*

---

## Abstract

We investigate the impact of sediment layers on ground motion characteristics during subshear and supershear rupture growth. Our findings suggest that sediment layers may lead to local supershear propagation, affecting ground motion, especially in the fault parallel (FP) direction. In contrast to homogeneous material models, we find that in the presence of sediment layers, a larger fault normal (FN) compared to fault parallel (FP) particle velocity jump, reflects shear propagation at depth but does not rule out shallow supershear propagation. Conversely, a large fault parallel (FP) compared to fault normal (FN) particle velocity jump indicates supershear propagation at depth. In the presence of a shallow layer, we also uncover a non-monotonic behavior in the sediment's influence on supershear transition and ground motion characteristics. During supershear propagation at depth we observe that sediment layers contribute to enhancing FP velocity pulses while minimally affecting the FN component. Furthermore, in the limit of global supershear propagation we identify local supersonic propagation within the sediment layers that significantly alters the velocity field around the rupture tip as observed on the free surface, creating both dilatational and shear Mach cones. In all our models with sediments we also find a significant enhancement in the fault vertical component of ground velocity. This could have particular implications for hazard assessments, such as in applications related to linear infrastructure, or a higher propensity to tsunami wave generation. Our research unravels the importance of considering heterogeneous subsurface material distribution in our physical models as they can have drastic implications on earthquake source physics.

**Keywords:** Supershear rupture, ground motion, sediment layers, dynamic rupture modeling

---

## 1. Introduction

Earthquake ruptures generate ground motions that pose significant hazards to buildings and infrastructure. In recent years, improvements in observational facilities have allowed researchers to identify several large strike-slip events. In these events, the near-source ground motion exhibits uncharacteristically large pulses. These examples include 1999 Mw7.6 Izmit (Turkey), 2002 Mw7.9 Denali (Alaska), 2016 Mw7.0 Kumamoto (Japan), and more recently the Kahramanmaraş Mw7.8 earthquake [1, 2, 3, 4, 5, 6, 7]. Such velocity pulses are usually captured only by near-fault stations. Examples include Pump station 10 for the 2002 Denali earthquake [8, 9, 10], and stations TK:NAR and KO:KHMN for the magnitude 7.8 Kahramanmaraş/Pazarcik earthquake [7, 6]. Several studies have attributed these velocity pulses to the passage of Mach fronts associated with supershear ruptures.

---

*Email address:* meguid@caltech.edu (Mohamed Abdelmeguid<sup>1</sup>)

Supershear earthquakes are earthquakes in which the rupture speed exceeds the shear wave speed of crustal rocks  $C_s$ . Such behavior has been observed both in the laboratory [11, 12, 13, 14, 10, 15, 16] and the field [10, 8, 17, 18, 9]. In a supershear rupture, the rupture propagation speed is faster than the shear wave speed. This difference in speeds results in the formation of a Mach front that moves faster than the seismic waves it generates. As previous studies have shown, the wave field generated by a propagating rupture is based on the propagation speed of the rupture front  $V_r$  relative to the shear wave speed  $C_s$ , favoring higher fault-parallel (FP) than fault-normal (FN) velocities at higher speed ratios  $V_r/C_s$  [14, 19, 1, 20]. Appendix A.1 illustrates the geometrical basis for this mechanistic signature.

Recent studies revealed that supershear ruptures may be more common than previously assumed [21, 22, 7, 1, 10, 23]. This has led to an influx of scientific investigations on various aspects of supershear ruptures, such as the effects of Earth’s free surface, stress state, and material heterogeneity. The Earth’s free surface significantly affects earthquake rupture dynamics. The presence of a free surface triggers free-surface-induced (FSI) supershear ruptures on strike-slip faults, facilitated by the generalized Burridge-Andrews mechanism [24, 25, 26, 27]. The role of material heterogeneity on the dynamics of supershear rupture propagation and its ground shaking has been a subject of extensive studies [28, 29, 30]. Low velocity fault zones that represent damaged regions surrounding faults have been found to promote pulse-like characteristics, enhance the frequency content of the ground shaking, and potentially lead to supershear transition [31, 32, 33, 29]. Other studies have explored the role of distributed material heterogeneity on Mach cone coherence for supershear earthquakes [34]. Despite all the attention that supershear ruptures have garnered, one aspect that remains understudied is the interaction between supershear rupture propagation and shallow sediment layers. While a previous study explored the role of sediment layer on the supershear transition length [35], the near-fault ground motion characteristics associated with either local (supershear propagation within the sediment) or global supershear (supershear propagation within both the sediment and bedrock) rupture in the presence of sediment basins remain largely unexplored.

Sedimentary basins tend to form along strike slip faults as a result of localized crustal deformations and are commonly found along major plate boundaries and mature faults [36, 37, 38]. It has been long acknowledged that the presence of shallow layers of softer material would amplify ground motion [39, 40]. An open question remains: what exactly are the characteristics of the resultant ground motion? Are the components only amplified? Or does the local heterogeneity interact with rupture propagation to alter the nature of the ground motion? This leads to another important aspect that remains unexplored, which is how the ground motion is influenced when the rupture propagation speed is higher than the shear wave speed within the sediment, but lower than that of the bedrock. It is thus important for both the engineering and geophysical communities to explore the ground shaking that is produced by each individual scenario.

To address these knowledge gaps, we aim to investigate the near-fault ground shaking associated with surface-breaking ruptures in the presence of shallow sediment layers. We will compare the ground motion characteristics of subshear ruptures in homogeneous and layered models, with a particular focus on the effects of shallow supershear propagation. Additionally, we will explore the parameter space leading to supershear transition in layered models and examine its implications for ground motion metrics.

We will simulate several scenarios using physics-based 3-D dynamic rupture models within a rate-and-state frictional framework [41, 42, 43]. Our goal is to provide insights into the potentially unique ground motion signatures that emerge in the near-fault region due to the presence of sedimentary layers and local supershear rupture propagation. Understanding these ground motion signatures may then inform the development of more accurate seismic hazard models.

In the following sections, we will describe our methodology in section 2. In subsection 3.1, we will explore the differences between a homogeneous case and a layered case with a mild material contrast. Within this model we explore two end-member cases of subshear and supershear propagation and compare the resultant ground motion characteristics. In subsection 3.2 we will repeat the previous exploration for a model with stronger material contrast. In subsection 3.3 we will compare key ground motion metrics for a homogeneous medium and a layered one focusing on quantities that influence the built environment response such as peak ground velocity, spectral accelerations, and Fourier amplitude spectrum. In section 4 we will discuss our results in the context of more realistic parameter distribution such as linearly varying material properties, or depth-dependent frictional variation. Furthermore, we will also explore the role of varying sediment

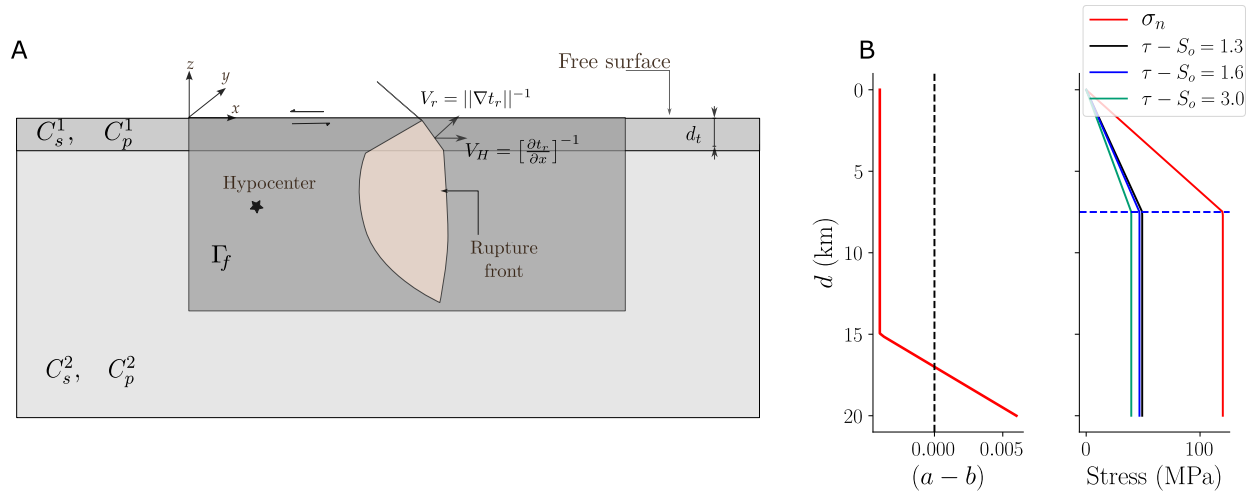


Figure 1: **The three-dimensional dynamic rupture model setup.** (a) Schematic of the simulation domain with sediment layer of depth  $d_t$ . A schematic representation of the rupture propagation along the fault surface showing the impact of the sediment layer on bending the rupture tip and altering the normal of the rupture front. The normal to the rupture front dictates the rupture speed  $V_r$ , which is calculated as highlighted in the schematic. (b) The distribution of depth-variable normal stress  $\sigma$ , shear stress  $\tau$ , and frictional parameters  $a - b$ .

thickness. Finally, in section 5 we will summarize our findings.

## 2. Model Setup

We consider a planar 2-D vertically dipping strike-slip fault embedded in a 3-D layered domain as shown in Figure 1a. We consider a single sediment layer of variable depth  $d_t$  km to evaluate the role of sediment depth on the ground motion. In our analysis, we only consider depth-varying stress and friction, and assume uniformity along the strike. At the rupture front, the actual rupture velocity  $V_r$  is defined as the propagation speed normal to the front and is given by  $V_r = \|\nabla t_r\|^{-1}$ , where  $t_r$  is the time of rupture arrival computed when the slip rate exceeds a specific threshold of 0.1 m/s. The horizontal rupture speed  $V_H$  is defined as  $V_H = [\partial t_r / \partial x]^{-1}$ .

The distribution of the depth-dependent effective normal stress is shown in Figure 1b and is numerically given as  $\sigma = \min[1.0 + 16.2z; 120.0]$  MPa, where  $z$  is in kilometers. The stress increases with depth due to the difference between overburden stress and the hydrostatic pore pressure and becomes constant (120.0 MPa) at depths larger than 7.4 km, due to the assumption that fluid over-pressure prevents further increase of  $\sigma$  with depth. The existence of depth-dependent variation in stress has important ramifications in 3-D simulations as it may result in rupture front complexity [26]. The bedrock pressure and shear wave speeds ( $C_p^2$  and  $C_s^2$ ) are chosen to be 6 and 3.46 km/s respectively. For wave speeds, the superscript  $(\cdot)^{1,2}$  will be used to distinguish the material properties of the sediment and bedrock respectively. The density of both the sediment and bedrock is chosen to be 2670 kg/m<sup>3</sup>.

The constitutive behavior is governed by a strong rate-weakening rate-and-state friction, in which the fault strength depends on both the rate of sliding and state evolution. The choice of a strong dynamic weakening response is motivated by experimental results that highlight a strong dependence on slip velocity at coseismic rates [44, 45, 46, 47, 48, 49, 50]. The distribution of frictional parameters along the depth is shown in Figure 1b.

The particular form of the steady-state coefficient of friction is given as [51]:

$$f_{ss} = f_w + \frac{f_{LV} - f_w}{\left[1 + (\dot{\delta}/V_w)^8\right]^{1/8}} \quad (1)$$

where  $\dot{\delta}$  is the sliding velocity, the velocity-weakening  $V_w$ , and fully weakened friction coefficient  $f_w$  are determined from laboratory experiments which suggest that  $V_w \sim 0.1$  m/s and  $f_w \sim 0.2$ .  $f_{LV}$  is the low velocity coefficient and is defined as:

$$f_{LV} = f_o - (b - a) \ln(\dot{\delta}/V_o) \quad (2)$$

We combine this strong rate-weakening friction with the regularized version of rate-and-state friction, where the friction coefficient is expressed as:

$$f(V, \Psi) = a \operatorname{asinh} \left( \frac{\dot{\delta}}{2V_o} e^{\frac{\Psi}{a}} \right) \quad (3)$$

The state variable  $\Psi$  evolves according to an evolution equation:

$$\frac{d\Psi}{dt} = -\frac{\dot{\delta}}{L} \left[ \Psi - \Psi_{ss}(\dot{\delta}) \right], \quad \Psi_{ss} = a \ln \left\{ \frac{2V_o}{\dot{\delta}} \sinh \left[ \frac{f_{ss}(\dot{\delta})}{a} \right] \right\} \quad (4)$$

The ruptures are nucleated by artificially forcing failure in a circular region (radius = 3 km) on the faults at depth  $d_H$  until spontaneous rupture propagation occurs. The perturbation in shear stress is mathematically smooth in both space and time and is conducted by smoothly increasing the shear stress within the circular patch over a time period  $t_{rise}$  as described in SCEC benchmark TPV-103.

The assumed variation of frictional parameters  $a - b$  with depth is shown in Figure 1. The seismogenic zone extends from 0 to 15 km. The closer the initial shear stress state on the fault to the interface strength, the more favorable the supershear transition becomes. This notion is captured by the fault strength term  $\mathcal{S}$  which quantifies the ratio of strength excess to dynamic stress drop  $\mathcal{S} = (\tau_p - \tau_o)/(\tau_o - \tau_r)$  [52, 53]. Lower values of  $\mathcal{S}$  have been shown to favor shorter supershear transition length for generalized Burridge Andrews mechanism [54, 55], and faster supershear saturation of the seismogenic zone for free-surface-induced supershear transition [56, 26]. This is because the transition length to supershear  $L_T$  is proportional to  $L_T \propto \mathcal{S} L_f$ , where  $L_f$  is the frictional length scale obtained from the frictional law [54]. In our models,  $L_f$  is kept constant and only  $\mathcal{S}$  is changed. Within rate-and-state friction, there are no well-defined a priori estimates for  $\tau_p$  and  $\tau_r$ . However, similar to Dunham et al. 2011, we obtain estimates for the peak strength ( $\tau_p$ ) and residual strength ( $\tau_r$ ), which we can later adjust given knowledge of the slip rate:

$$\tau_p \approx \sigma_n \left[ a \ln(\dot{\delta}_{co}/V_o) + \Psi_o \right], \quad \tau_r \approx \sigma_n \left[ f_{ss}(\dot{\delta}_{co}) \right] \quad (5)$$

Here,  $\dot{\delta}_{co}$  is the co-seismic slip velocity, assumed to be  $\sim 10$  m/s, which is consistent with observed slip velocities during dynamic rupture simulations. In our study, we fix the value of the initial peak friction coefficient (given as  $\tau_p/\sigma_n$ ) to be  $\sim 0.72$  for all simulations by setting  $\Psi_o = 0.56$ . We then vary the  $\mathcal{S}_o$  parameters in our simulations by changing the background stress  $\tau_o$ .

All the simulations in this work are conducted using an open-source software DRDG3D, which was developed by Zhang et al. (2023) for dynamic rupture modeling. DRDG3D adopts an upwind/central mixed flux scheme, which removes numerically generated artificial oscillations. The numerical efficiency and accuracy of DRDG3D are documented in [57].

### 3. Results

In this study we are interested in understanding the ground motion characteristics of sub-shear and supershear ruptures in the presence of a shallow sediment layer. We will explore how those characteristics change with varying material contrast  $C_s^1/C_s^2$ , the depth of the sedimentary layer, and the initial value of the strength parameter  $\mathcal{S}_o$ . To focus on the effect of the sediment in this initial study, we will primarily consider a single sediment layer on top of a homogeneous half-space. We consider two contrast ratios  $C_{s,p}^1/C_{s,p}^2$  equal to 70% and 50%. Throughout the study,  $C_{s,p}^2$  remains fixed while we vary  $C_{s,p}^1$ . Within each contrast ratio, we consider end member cases of the strength parameter  $\mathcal{S}_o = 3$  and  $\mathcal{S}_o = 1.6$ . Finally, we will study the

influence of sediment layers on key ground motion metrics by focusing on two models, one that is subshear  $\mathcal{S}_o = 3$ , and one that is supershear  $\mathcal{S}_o = 1.3$ . We chose a slightly smaller  $\mathcal{S}_o$  to guarantee rapid supershear transition in both the homogeneous and the sediment models. A summary of all the models considered in this study is provided in Table 1.

Table 1: The different models considered in this study with varying sediment material properties, depth, initial stress state.

	<b>Contrast</b>	$\mathcal{S}_o$	$d_t$
<b>Homogeneous Models</b>			
	$C_p^1 = C_p^2, C_s^1 = C_s^2$		
H-1		3	
H-2		1.6	
H-3		1.3	
<b>Mild Contrast Models</b>			
	$C_p^1 = 0.7C_p^2, C_s^1 = 0.7C_s^2$		
A-1		3	2
A-1*		3	5
A-2		1.6	2
A-2*		1.6	5
A-3		1.3	2
<b>Strong Contrast Models</b>			
	$C_p^1 = 0.5C_p^2, C_s^1 = 0.5C_s^2$		
B-1		3	2
B-1*		3	5
B-2		1.6	2
B-2*		1.6	5
<b>General Models</b>			
LVS-1	Linear velocity structure [58]	3	varies
LVS-2	Linear velocity structure [58]	1.6	varies
A-1 <sup>VS</sup>	$C_p^1 = 0.7C_p^2, C_s^1 = 0.7C_s^2$	3	2
A-2 <sup>VS</sup>	$C_p^1 = 0.7C_p^2, C_s^1 = 0.7C_s^2$	1.6	2

<sup>VS</sup> superscript *VS* indicates a model with a velocity-strengthening portion near the free surface.

### 3.1. Mild material contrast $C_{s,p}^1 = 0.7C_{s,p}^2$

Our starting point is a case with a mild (70%) shear and pressure wave speed contrast between the bedrock and the sediment. The depth of the sediment is chosen as  $d_t = 2$  km. We will refer to this Model as A.

#### 3.1.1. Large fault initial fault strength ratio $\mathcal{S}_o = 3$ (A-1):

In Figure 2a we show snapshots of the rupture propagation. The rupture nucleates within the overstressed patch, then expands until it saturates the seismogenic zone, and proceeds to propagate along the x-direction. The rupture front bends within the sediment layer due to the lower wave speeds in that medium (as shown in the zoomed-in snapshot). This results in a change in the rupture front speed  $V_r$ , which is computed based on the normal to the rupture front. At later times between  $t = 18.0$  and  $23.1$  s, the rupture propagates steadily with an identical slip rate profile. Based on propagation distances ( $\sim 15$  km) within the last two snapshots (5.1 s), the rupture propagation speed is  $V_r = 3$  km/s, which is indeed “subshear” based on the bedrock shear wave speed.

The resultant near-fault ( $< 12$  km away from the source) particle velocity field generated by this propagation is shown in Figure 2b. We show the fault-parallel (FP) particle velocity wave field at times  $t = 18.0$  and  $23.1$  s respectively after rupture nucleation. We observe the emergence of a Mach cone structure within the velocity field near the rupture tip. The emergence of the Mach cone is a signature of supershear rupture propagation. As mentioned earlier, the rupture is subshear within the bedrock, so the emergence of

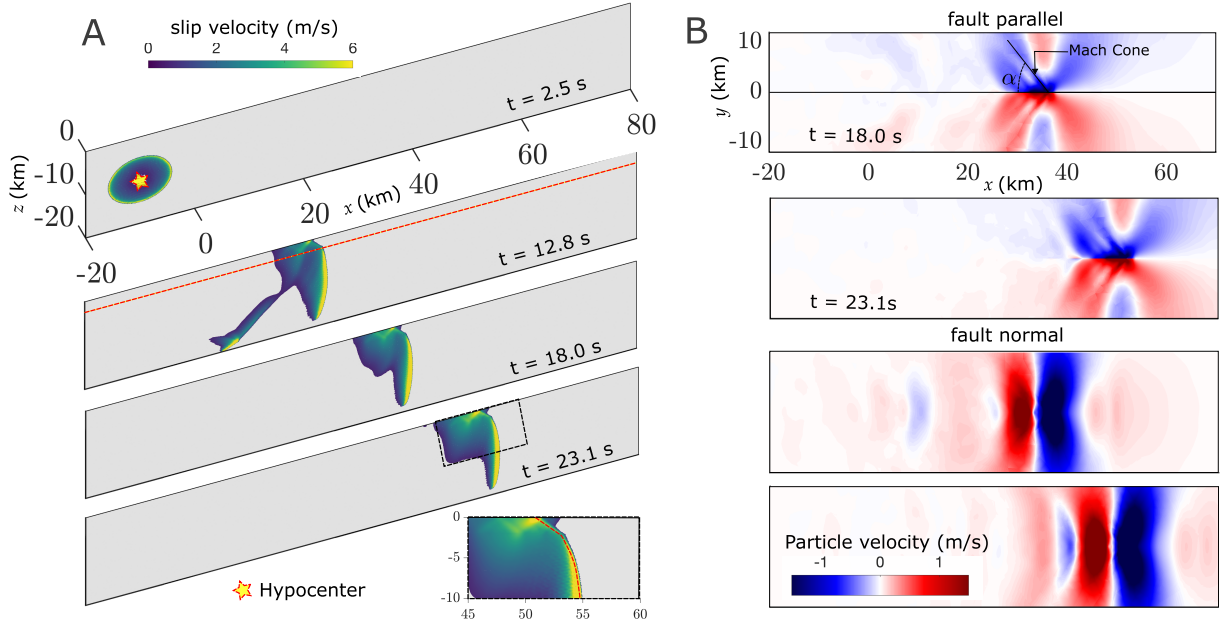


Figure 2: **The role of sediment layer contrast in altering rupture propagation and ground motion characteristics for Model A-1.** (a) snapshots of the rupture propagation at different times ( $t = 2.5, 12.8, 18.0$  and  $23.1$  s). (b) Contours of the fault-parallel and fault-normal particle velocity wave-field within near field of the fault at later stages of rupture propagation ( $t = 18.0$  s, and  $t = 23.1$  s).

a Mach cone is attributed to local supershear propagation within the sediment. The Mach cone has an angle  $\alpha \approx 52^\circ$ . Despite being supershear, a Mach cone angle  $\alpha_s > 45^\circ$  indicates a sub-Eshelby propagation speed. Sub-Eshelby propagation speed is characterized by a propagation speed of  $V_r, V_H < \sqrt{2}C_s$ . We note here that some literature refers to rupture propagation between  $C_s$  and  $\sqrt{2}C_s$  as unstable supershear propagation [52, 59, 55, 60], but that is based on 2D analyses and does not extend to 3D propagation in a heterogeneous media or with complex fault geometry [61]. Furthermore, sub-Eshelby propagation has been observed in the field [21]. Because of the geometrical considerations, supershear ruptures propagating below the Eshelby speed *don't* have a fault-parallel (FP) particle velocity jump that is larger than the fault-normal (FN) particle velocity jump. In subsequent discussions, we will correlate the Mach cone angle with the horizontal rupture velocity  $V_H$  rather than the actual rupture speed within the sediment  $V_r$ . This is because the structure of the Mach cone at the free surface depends on the stress field generated by the rupture tip on the free surface, which is propagating at  $V_H$ . This is consistent with an earlier study by Hu et al. 2021, which also found that the Mach cone angle depends on the 1-D horizontal  $V_H$  speed rather than  $V_r$  [26]. Examining the fault-normal velocity wave field shown in Figure 2b at different times, we observe the characteristic “butterfly” structure associated with sub-shear propagation.

The emergence of the Mach cone within the FP component can be explained by examining the rupture propagation speeds within both the sediment layer and the bedrock, as shown in Figure 3. In Figure 3a, the mean and maximum values of the rupture speed  $V_r$  within the sediment layer are plotted. In the shaded region which coincides with the hypocentral location, the rupture speed exceeds the Eshelby speed ( $\sqrt{2}C_s^l$ ). This is due to a geometric effect that accelerates the rupture propagation speed to satisfy the boundary condition at the instance the rupture front encounters the free surface. We observe a strong scatter in the rupture propagation speed within the sediment layer for the fault segment given by  $0 < x < 50$  km. As the rupture propagates further,  $x > 50$  km, the scatter decreases. More importantly, both the mean and maximum values of  $V_r$  exceed the shear wave speed of the sediment layer at certain points during the rupture propagation. This increase in rupture propagation speed relative to the local wave speed explains the emergence of the Mach cone at the free surface. Both quantities stay below the local Eshelby speed

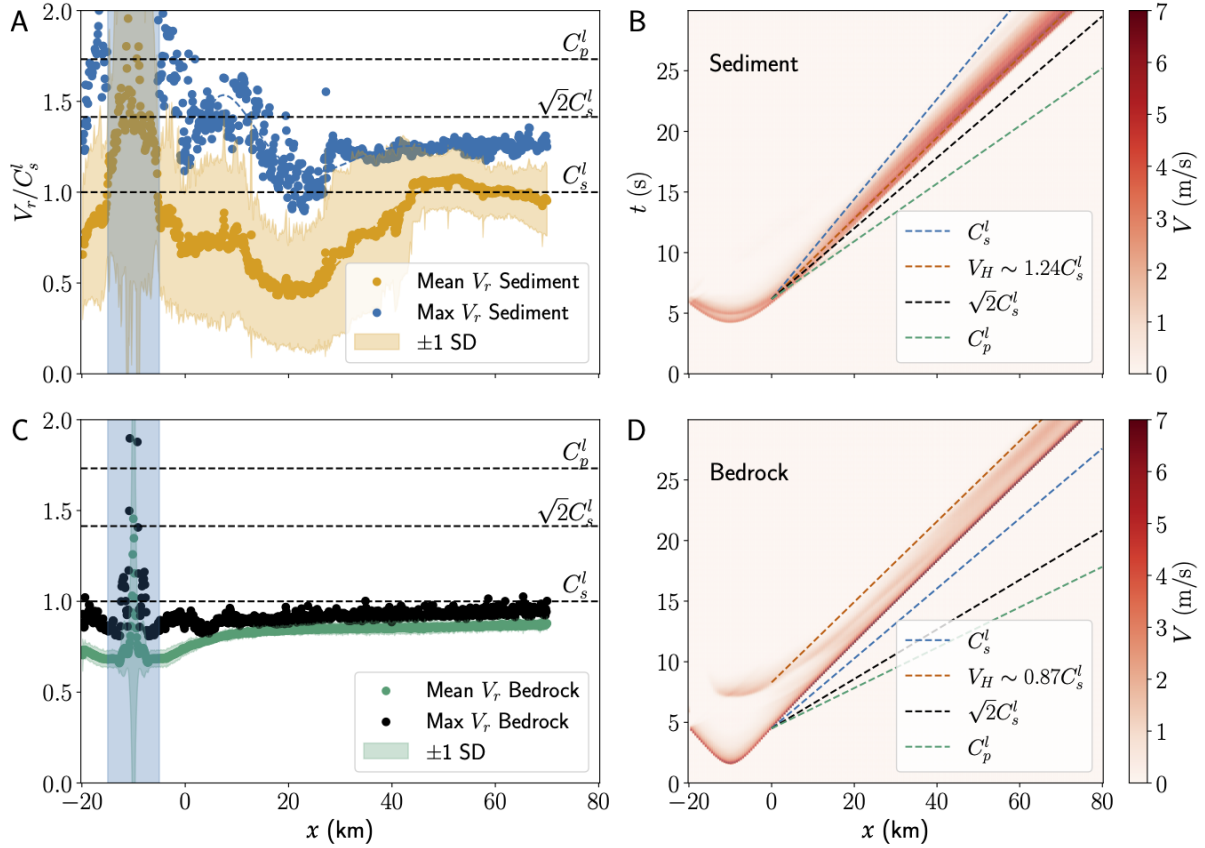


Figure 3: **The rupture propagation speeds in Model A-1** (a-b) Mean and maximum rupture propagation speed  $V_r$  within both the sediment and the bedrock. The shaded area represents the nucleation site of the rupture. (c-d) Spatiotemporal slip rate distribution at depth -1 km, and -7.5 km respectively to highlight local horizontal propagation speed  $V_H$  relative to local characteristics speeds  $C_s^l$ ,  $C_p^l$ , and  $\sqrt{2}C_s^l$ .

which is consistent with  $\alpha > 45^\circ$  seen in Figure 2b. Within the bedrock, as shown in Figure 3b, both the maximum and mean  $V_r$  stay below the shear wave speed of the bedrock. This is consistent with the subshear rupture propagation observed in Figure 2a.

The horizontal propagation speed  $V_H$  is tracked by plotting the spatio-temporal evolution of the slip pulse within the sediment at  $z = -1$  km and bedrock at  $z = -7.5$  km (Figure 3c-d). In Figure 3c, we estimate  $V_H \sim 1.24C_s^l$ , which is larger than the shear wave speed but smaller than the Eshelby speed. The supershear  $V_H$  further justifies the emergence of Mach cones at the free surface. Within the bedrock shown in Figure 3d, we estimate  $V_H \sim 0.87C_s^l$ , which is still subshear.

With knowledge of rupture speeds, we can independently estimate the Mach cone angle  $\alpha$ . Geometrically, the angle of the Mach cone is defined through the propagation speed as  $\alpha = \sin^{-1}(C_s^l/V_H)$ . Here, we use  $V_H$  because, as discussed earlier,  $V_H$  correlates better with free surface Mach cone when  $V_r \neq V_H$ . The rupture at depth, which is subshear, propagates with a speed  $V_H \sim 0.87C_s^l$ . For the given contrast, we predict the angle of the Mach cone as  $\alpha = \sin^{-1}(0.7/0.87) = 54.5^\circ$ , which is indeed very close to the observed angle of  $52^\circ$  at the free surface. Note here that we can also use  $V_H = 1.24C_s^l$  directly to obtain the same solution. The difference is merely the scaling by the contrast ratio. This interchangeability implies the horizontal rupture speed is constant with depth, which is also consistent with the unchanged curvature of the rupture front seen in Figure 2a once the rupture saturates the seismogenic zone at  $t > 12.8$  s. This observation indicates that measurements of the horizontal rupture speed  $V_H$  at the free surface are indicative of the rupture speed  $V_r$ .

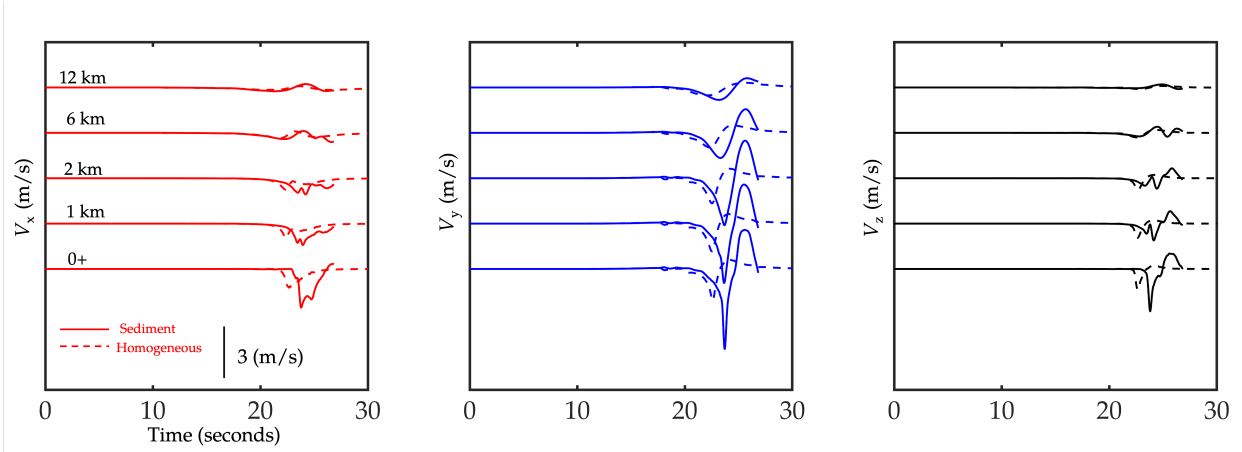


Figure 4: **The role of sediment layer contrast in altering synthetic ground motion characteristics for Model A-1** (a) Fault-parallel (FP), (b) fault-perpendicular (FN) and (c) vertical velocity time histories at five different sites. Sites are located at 50 km along strike and at distances ( $0^+$ , 1, 2, 6, 12) along the fault perpendicular direction.

at larger seismogenic depth. Accordingly, assuming continuous propagation in heterogeneous media, if we measure the rupture speeds on the surface using rupture phase tracking (which typically tracks horizontal rupture speeds), we can readily extrapolate to identify rupture speed at depth by using appropriate wave speed conversion.

In Figure 4, we plot the synthetic ground motion records for several stations located at  $x = 50$  km along strike and at multiple distances along the fault perpendicular direction ( $y = 0^+$ , 1, 2, 6, 12). In the very near field  $< 2$  km, we observe that amplification occurs in all three velocity components for the model with sediment (shown as solid line) in comparison to the homogeneous model (shown as the dashed black line). At distances larger than 6 km, the extent of amplification for the fault-normal (FN) component is larger than the fault-parallel (FP) and the vertical component.

To understand the nature of the ground motion amplification, we examine the possible sources that contribute to it:

1. Amplification may occur due to wave conversion and reflections at the interface between the bedrock and the sediment. Within the near-fault velocity field, wave conversion will have a relatively small contribution due to the low contrast ratio between the bedrock and sediment. Wave conversion will not explain a three times increase in the component's amplitude in the near-fault records [62]. At distances far away from the source, we expect such conversion to be more obvious.
2. Rupture propagation within a softer sediment layer will enhance slip rate, which will consequently result in higher ground particle velocities. As discussed in Mello et al. 2014, the steady-state velocity field  $\mathbf{v}$ , under 2D plane strain conditions, may be represented by [10]:

$$\mathbf{v} \left( \frac{x}{L}, \frac{y}{L} \right) = \hat{v}_0 \mathcal{F} \left( \frac{x}{L}, \frac{y}{L}, \frac{R}{L}, \frac{V_r}{C_s} \right) \quad (6)$$

where,  $\hat{v}_0 = C_s \frac{(\tau_p - \tau_r)}{\mu}$

Here,  $\mu$  is the shear modulus, and in Equation 6 the amplitude of the velocity field given by  $\hat{v}_0$  is  $\propto 1/\sqrt{\mu}$ . This proportionality implies that if the material is softer (i.e., lower  $\mu$ ), the amplitude of the velocity field will be higher, assuming that the ratio  $V_r/C_s$  remains constant. The role of  $V_r/C_s$  will be discussed in the subsequent point.

3. Near-fault amplification associated with rupture tip propagation speed. The stress concentration factor and the resulting stress field for a dynamically propagating slip pulse depend on the ratio of the rupture

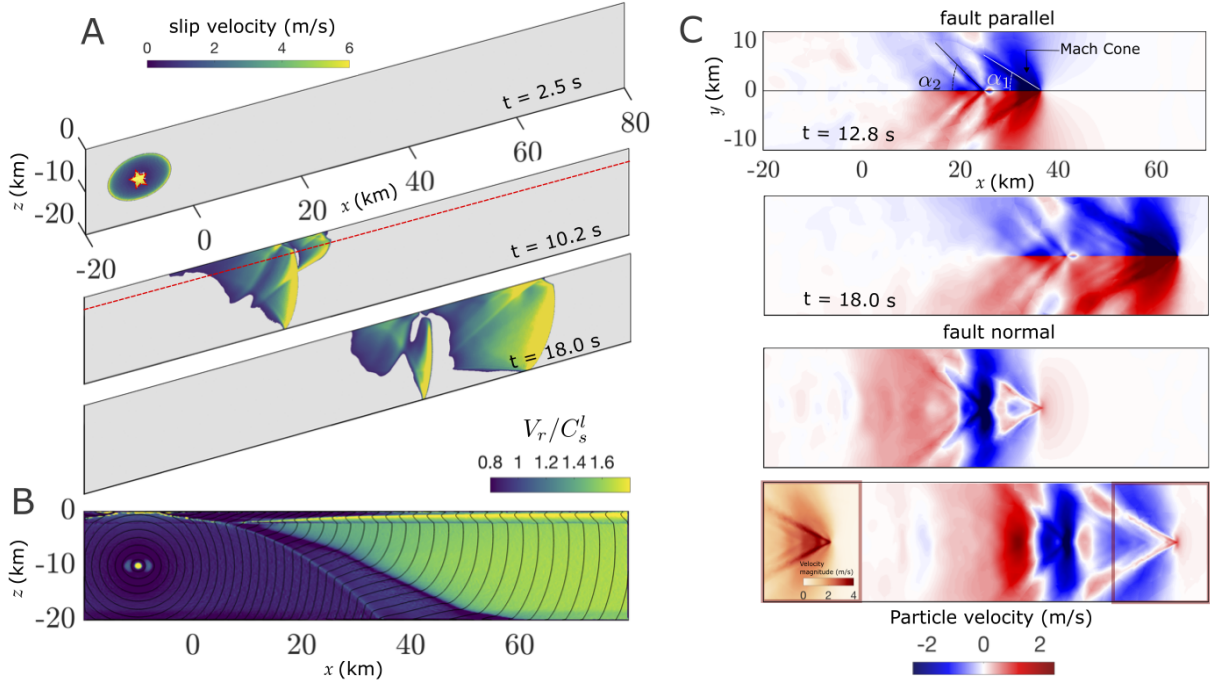


Figure 5: **The role of sediment layer contrast in altering rupture propagation and ground motion characteristics for Model A-2.** (a) snapshots of the rupture propagation at different times ( $t = 2.5$ ,  $10.2$ , and  $23.1$  s). (b) Contour of the normalized rupture speed  $V_r/C_s^l$ . (c) Contours of the fault-parallel and fault-normal particle velocity wave-field within near field of the fault at later stages of rupture propagation ( $t = 12.8$  s, and  $t = 18.0$  s). Zoomed figure in last panel shows the particle velocity magnitude near the rupture tip at  $t = 18.0$  s to highlight the structure of the Mach cone.

speed to the local characteristic wave speeds. We can observe this dependence within Equation 6 in the term  $\mathcal{F}$ . Since the rupture is propagating at the same  $V_H$  within the sediment and bedrock but the local wave speed is lower in the sediment, that ratio thus increases. This increase explains the emergence of the Mach cone seen in Figure 2. Furthermore, this increase in the rupture speed ratio changes the stress field generated near the rupture tip, potentially amplifying, or dampening the ground motion.

In subsequent sections, we will explore the role of the third contribution further.

### 3.1.2. Small fault strength ratio $\mathcal{S}_o = 1.6$ (A-2):

Next, we consider a case with a fault strength ratio  $\mathcal{S}_o = 1.6$ . This smaller choice of  $\mathcal{S}_o$  favors the transition to supershear rupture speeds in a homogeneous model (shown in Figure A.2) and within the bedrock for a model with sediment layer. We will refer to this as Model A-2.

In Figure 5a we show snapshots of the slip velocity at times  $t = 2.5$ ,  $10.2$ , and  $18$  s respectively. At  $t = 10.2$  s we observe the emergence of a secondary crack ahead of the rupture tip. This secondary crack then becomes the leading rupture tip propagating at a speed that exceeds the shear wave-speed within both the sediment and the bedrock. To highlight this transition, we plot the propagation speed  $V_r$  normalized by the local shear wave speed in Figure 5b. We observe that the rupture transitions to supershear speed  $V_r/C_s^l > 1$  within both the bedrock and the sediment. Furthermore, we observe that the normalized rupture speed is higher within the sediment versus the bedrock. Compared to the homogeneous case (shown in Figure A.2), for model A-2 we observe that the transition to supershear occurs much earlier, which implies that the sediment assisted in the supershear transition. This is potentially possible due to the heterogeneous P-SV conversion at both the free surface as well as the bedrock-sediment interface [56, 35].

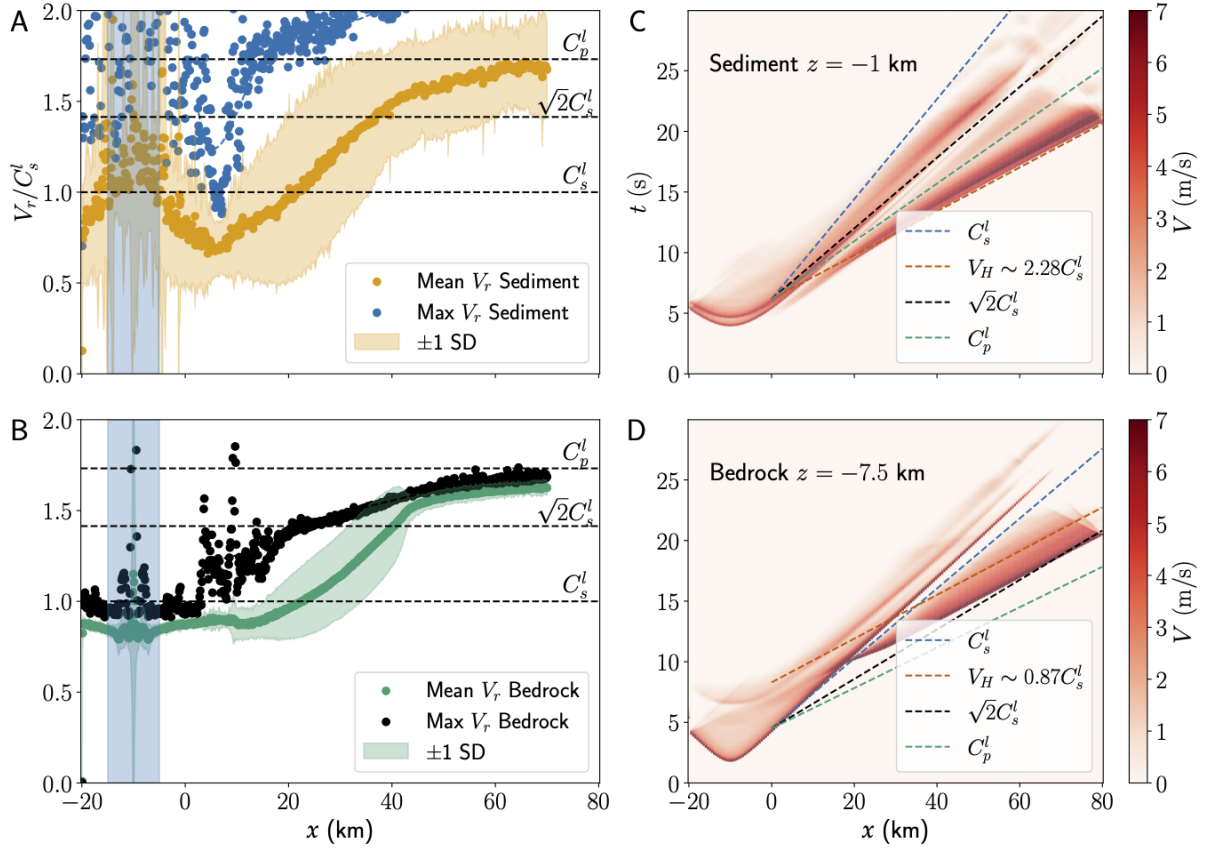


Figure 6: **The rupture propagation speeds in Model A-2** (a-b) Mean and maximum rupture propagation speed  $V_r$  within both the sediment and the bedrock. The shaded area represents the nucleation site of the rupture. (c-d) Spatiotemporal slip rate distribution at depth -1 km, and -7.5 km respectively to highlight local horizontal propagation speed  $V_H$  relative to local characteristics speeds  $C_s^l$ ,  $C_p^l$ , and  $\sqrt{2}C_s^l$ .

Figure 5c illustrates the particle velocity wave field for Model A-2. Within the FP component, we observe two distinct Mach cone signatures associated with (a) global supershear propagation (referring to supershear in both sediment and bedrock) with a Mach cone angle  $\alpha_1$ , and (b) local supershear propagation within the trailing subshear signal which has a Mach cone angle  $\alpha_2$ . The difference in angles is because the lead tip and the trailing one are propagating at different speeds relative to the local wave speeds. We further note that  $\alpha_2$  observed in Model A-2 is smaller than the  $\alpha$  observed in Model A-1 despite both being associated with a sub-shear rupture at depth. This is due to the trailing Rayleigh propagating at speeds faster than that of the subshear rupture in Model A-1.

The FN component undergoes a minor change at the leading rupture tip which is propagating in both the sediment layer and the bedrock at supershear speed. This is a typical signature of supershear propagation when the rupture speed exceeds the Eshelby speed, as illustrated graphically in Figure A.2. As the rupture accelerates, the Mach cone angle  $\alpha$  decreases and, consequently, the FN velocity perturbation carried by the Mach cone also decreases. The primary velocity pulse in the FN arrives at a later time with the trailing Rayleigh signature. We also note that the local supershear propagation in conjunction with wave reflections alters the form of the FN component relative to what is observed in Figure 2b.

The rupture propagation speed characteristics are shown in Figure 6. We observe that the mean  $V_r$  within both the sediment and the bedrock exceed the Eshelby speed. Interestingly, the maximum  $V_r$  in the sediment exceed the local pressure wave speed  $C_p^l$ . That is not the case for the bedrock as shown in

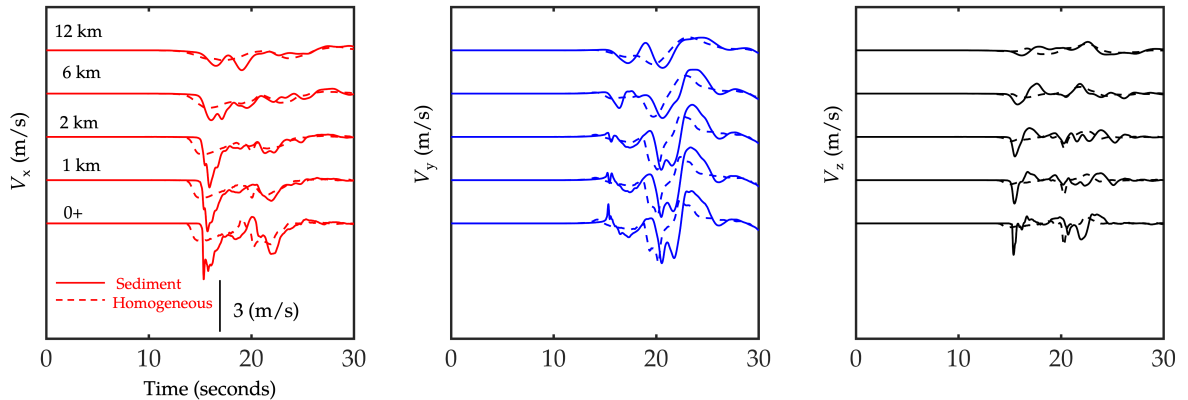


Figure 7: The role of sediment layer contrast in altering rupture ground motion characteristics for case with  $\mathcal{S}_o = 1.6$ . (a) Fault-parallel (FP), (b) fault-perpendicular (FN) and (c) vertical velocity time histories at five different sites. Sites are located at 50 km along strike and at distances ( $0^+$ , 1, 2, 6, 12) along the fault perpendicular direction.

Figure 6B. The slip pulse propagation speeds  $V_H$  is estimated in Figure 6C-D to be  $\sim 2.27C_s^l$  within the sediment and  $\sim 1.6C_s^l$  with in the bedrock. Note, that the difference is due to scaling of  $C_s^l$ . Similar to Model A-1 this implies that  $V_H$  is the same with the bedrock and the sediment. The observation of similar  $V_H$  within the sediment and the bedrock is purely geometric. It emerges because for the rupture front to retain its curvature after saturating the seismogenic zone (steady state), the horizontal rupture speed at the free surface has to match the rupture speed at the interface between the bedrock and the sediment. It is important to emphasize that there is no physical justification for the rupture front curvature to change within the sediment layer, since locally the material is homogeneous, the stress field varies linearly, and the propagation path is unhindered.

This *apparent* supersonic propagation driven by the rupture process at depth in conjunction with the local supershear propagation within the sediment layer led to multiple Mach cones observed within the velocity field shown in Figure 5C. We also observe that the trailing Rayleigh pulse is propagating at speeds slightly below the local Esheby speed which explains the wider Mach cone angle seen in Figure 4B. At a depth of 7.5 km within the bedrock, a leading slip pulse is observed propagating at supershear speed relative to the local speeds. Furthermore, at depth 1, and 7.5 km we observe that the lead slip pulse propagating horizontally at the same speed  $V_H$ . This is similar to model A-1 where the speed within the sediment is directly equivalent to the speed at depth.

In Figure 7, we plot synthetic velocity field records for stations located at  $x = 50$  km along strike and at multiple distances in the fault perpendicular direction ( $y = 0^+$ , 1, 2, 6, 12). Within the synthetic near-fault records, we observe larger fault-parallel (FP) than fault-normal (FN) velocity jumps associated with the leading rupture tip. *This implies that 2-D conclusions regarding velocity jumps hold true in the case of the global supershear condition, even in the presence of material heterogeneity.* At later times, we observe a secondary pulse associated with the trailing Rayleigh signal and the local supershear. In the secondary pulse, the FN component dominates the FP component. The fault-normal component shows a clear lack of amplification compared to the homogeneous case. It is also worth noting that the FN component is smaller than that observed in Model A-1. In the vertical component  $V_z$ , we observe a substantially large amplification that is absent in the homogeneous case, arriving with the leading rupture tip.

In Figure 4, for Model A-1, we observe a strong amplification of the FN component relative to the homogeneous case. However, for Model A-2 shown in Figure 7, there is almost no amplification for either the leading rupture field or the trailing one. To better understand this observation, we study the steady state characteristics of a crack propagating at supershear speed. The approximation of a steady state is well justified by the fact that at later times (a) the rupture has fully saturated the seismogenic zone with

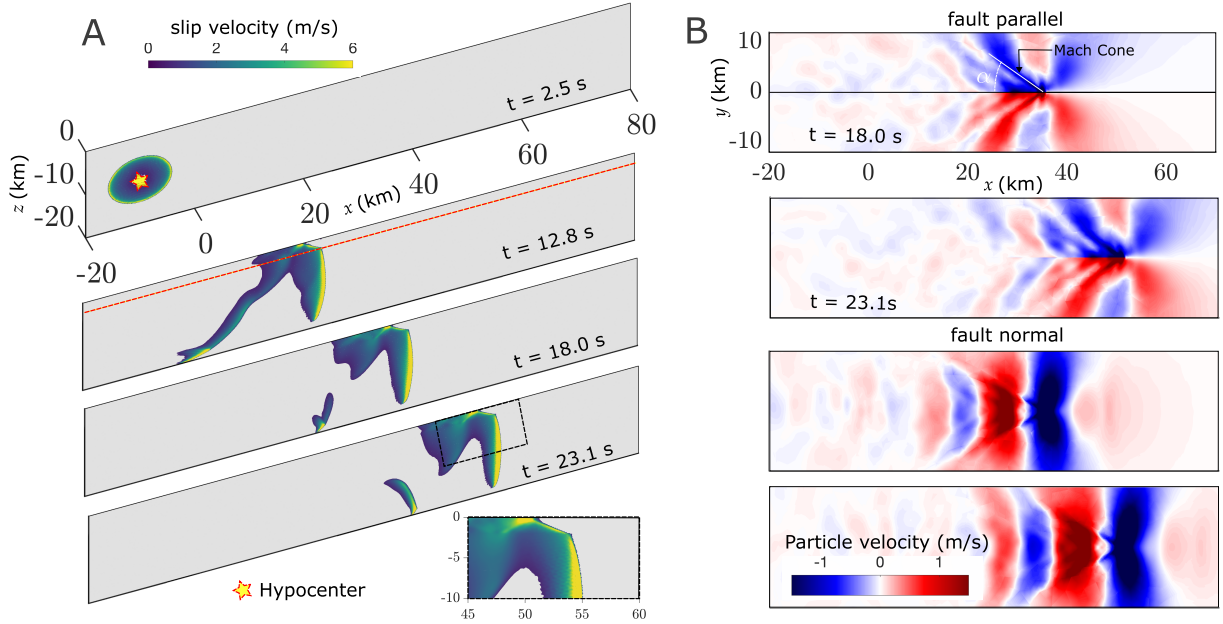


Figure 8: **The role of sediment layer contrast in altering rupture propagation and ground motion characteristics for Model B-1.** (a) snapshots of the rupture propagation at different times ( $t = 2.5, 12.8, 18.0$  and  $23.1$  s). (b) Contours of the fault-parallel and fault-normal particle velocity wave-field within near field of the fault at later stages of rupture propagation ( $t = 18.0$  s, and  $t = 23.1$  s).

no along-strike variations in stress, geometry, or frictional properties, and (b) there is sufficient separation between the leading tip and the trailing one. We can then express the fault-normal velocity field during local supershear as [63, 20, 10, 14]:

$$V_y = \mathcal{M}(\beta_s) \dot{\delta} = \frac{-1}{\beta_s} \left[ \frac{1}{2} - \frac{1}{\beta_s^2 + 1} \right] \dot{\delta} \quad (7)$$

In Equation 7, we separate the contributions of the slip rate and the rupture speed. Based on Figure 6C and Figure 3C, the slip rate of the trailing Rayleigh is similar between models A-1 and A-2. Thus in order to understand the difference between Model A-1 and Model A-2, we need to examine how the term  $\mathcal{M}$  varies between the two models. It is important to note that under those conditions the limit of  $V_H \rightarrow \sqrt{2}C_s^l$ ,  $\mathcal{M} \rightarrow 0$ . This implies that as we approach Eshelby speed, the velocity pulse carried by the Mach cone in the fault-normal component should technically vanish.

In Model A-1, as shown in Figure 3, the propagation speed of the slip pulse is sub-Eshelby ( $V_H \sim 1.24$ ,  $\beta_s = 0.733$ ). In Model A-2, the trailing rupture, that is propagating at locally supershear speed and carries the dominant fault-normal velocity pulse, accelerates toward the Eshelby speed ( $V_H \sim 1.35$ ,  $\beta_s = 0.91$ ). This increase in  $\beta_s$ , as the rupture accelerates, leads to a decrease in the magnitude of  $\mathcal{M}$  and, consequently, the magnitude of the fault-normal velocity pulse carried by the Mach cone. This change is independent of the contribution of the slip rate which is similar between the two models. This observation highlights the importance of the changing rupture characteristics on near-fault ground motion.

### 3.2. Strong material contrast $C_s^1 = 0.5C_s^2$

#### 3.2.1. Large fault strength ratio $\mathcal{S}_o = 3$ (B-1):

In Figure 8 we show model B-1 with 50% contrast to explore the role of increasing material contrast. We again start by exploring the large strength ratio case of  $\mathcal{S}_o = 3$ . We note that 50% might be quite a

large contrast for a 2 km deep shallow sediment. However, such high contrast would emphasize the potential differences when compared to the homogeneous case.

In Figure 8a we show snapshots of the slip rate on the fault surface. In comparison with Model A-1, we observe similar rupture propagation characteristics with a minor difference in the orientation of the rupture front normal within the sediment (shown in zoomed-in panel Figure 8a). This change is attributed to the softer sediment altering the curvature of the rupture front. The rupture propagation speed within the bedrock is still sub-shear, and it is the same as observed in Model A-1. Similar to Model A-1, we observe that the rupture front is still straight. To maintain this front geometry, the rupture tip consequently must propagate at the same horizontal rupture speed in both the sediment and the bedrock.

By examining the ground particle velocity wave-field in the near field of the fault, we again observe the emergence of a Mach cone within the FP component. The Mach cone angle  $\alpha$  is smaller than the one observed in Model A-1. Furthermore, the Mach cone also has a wider extent. From the ground particle velocity field, we estimate the Mach cone angle to be approximately  $\alpha \sim 35^\circ$ . Despite the rupture propagation speed at depth being the same in both Models A-1 and B-1, the structure of the Mach cone at the surface is different. This is due to the difference in propagation speeds relative to the local shear wave speed. Here, because of the larger contrast, there is a clear separation between the leading rupture tip and the reflections that emerge at the interface between the sediment and the bedrock. This separation leads to the emergence of a secondary pulse trailing the leading rupture tip. Furthermore, since the secondary pulse is also propagating at a speed faster than the local shear wave speed, it generates a Mach cone.

We examine the rupture propagation speeds in Figure 9. In Figure 9a, we observe that the mean rupture speed  $V_r$  exceeds the local shear wave speed  $C_s^l$  in the distance range  $x = 40$  to 70 km. Furthermore, the maximum  $V_r$  exceeds the local Eshelby speed. Within the bedrock, as shown in Figure 9b, the rupture propagation speed is subshear and is similar to Model A-1 shown in Figure 3b. The spatio-temporal evolution of the slip rate shows a similar pattern. The horizontal rupture propagation speed  $V_H$  exceeds the local Eshelby speed and is almost equal to the local pressure wave speed  $C_p^l$ , which coincides with the maximum value of  $V_r$  within the sediment. Within the bedrock, the propagation speed  $V_H$  is still subshear at  $0.87C_s^l$ . Similar to Model A-1, we can back-calculate the Mach cone angle using these rupture speed estimates. For  $V_H = 1.73C_s^l$  in the sediment, the estimated Mach cone angle  $\alpha = 35.3^\circ$ , which is in agreement with the Mach cone angle observed in the particle velocity field.

Within the synthetic ground motion records shown in Figure 10, we observe that the FP component jump becomes almost comparable to the FN component jump within the near-fault record  $0^+$ . However, despite having a Mach cone angle lower than  $45^\circ$ , the FP is not the dominant component even at  $0^+$ . Combined with the observations in Model A-1, *this implies that FN > FP jump may not rule out local supershear propagation. However, an FN > FP remains indicative of a dominant subshear propagation at depth.* We note here that, unlike global supershear rupture, there is no clear separation between the rupture tip and the trailing Rayleigh signature, which means that the ground motion signature is a superposition of a strong subshear component (at depth) and the local supershear effects (within the sediment), which would contribute to why the condition of FP > FN is not satisfied.

Furthermore, we observe secondary pulses in the FP component associated with the second Mach cone. Both FP pulses attenuate with fault perpendicular distance. Another important observation when comparing the role of material contrast is that despite a clear increase in contrast from Model A-1 to B-1, the increase in the contrast primarily affected the FP component with no apparent further amplification of the FN component. This is due to the competition between amplification by propagation through a softer material and dampening due to altered rupture propagation speed as discussed in the previous section.

### 3.2.2. Small fault strength ratio $\mathcal{S}_o = 1.6$ (B-2):

Similar to models A, we also explore a smaller initial fault strength ratio  $\mathcal{S}_o$  to investigate the implications of having a sediment layer on global supershear propagation. We refer to this model as B-2. In Figure 11a we again observe an earlier supershear transition relative to the homogeneous model for model B-2.

Within the velocity field, we see similar features to model A-2. However, due to the softer media, we observe the emergence of multiple Mach cones. The Mach cones' angles are different between the leading

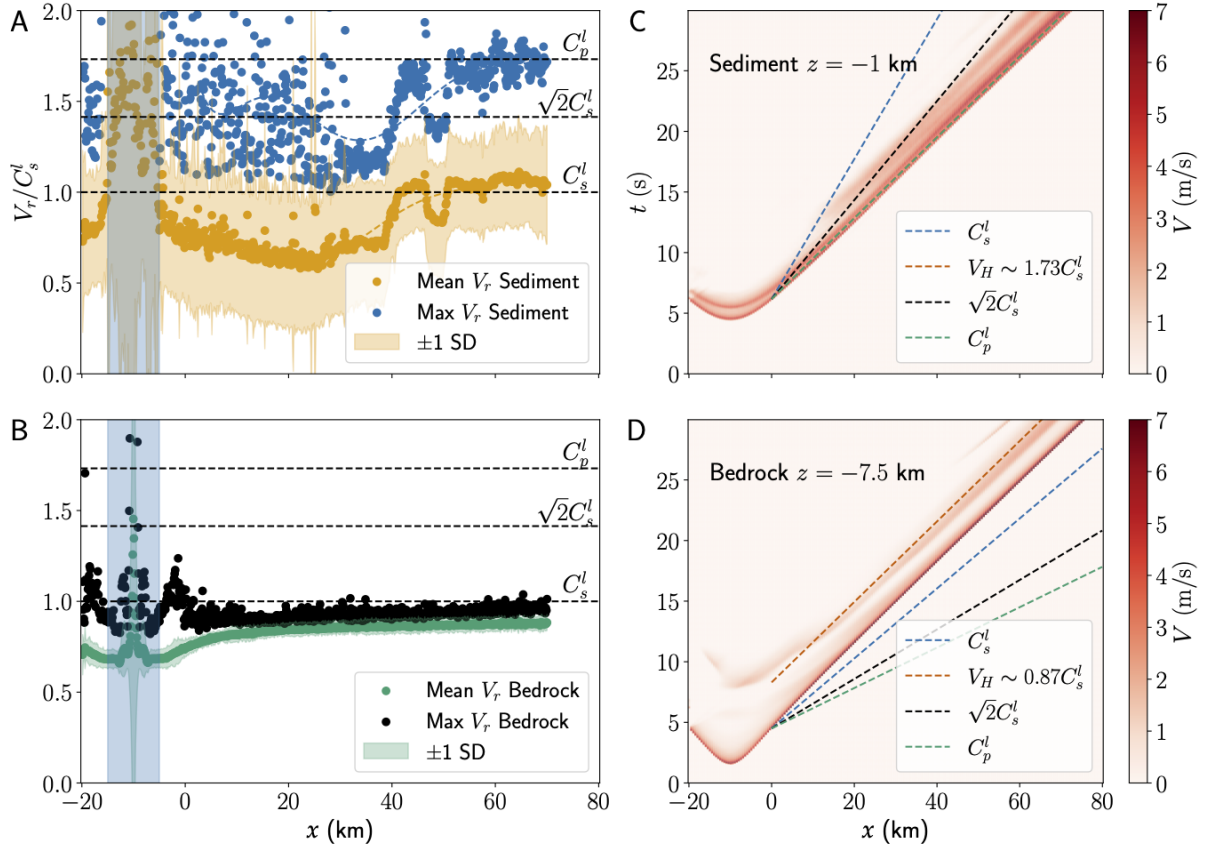


Figure 9: **The rupture propagation speeds in Model B-1** (a-b) Mean and maximum rupture propagation speed  $V_r$  within both the sediment and the bedrock. The shaded area represents the nucleation site of the rupture. (c-d) Spatiotemporal slip rate distribution at depth -1 km, and -7.5 km respectively to highlight local horizontal propagation speed  $V_H$  relative to local characteristics speeds  $C_s^l$ ,  $C_p^l$ , and  $\sqrt{2}C_s^l$ .

tip and the subsequent trailing signature. These Mach cones are associated with (1) local supershear propagation, and (2) reflected waves at the sediment-bedrock interface that now have sufficient separation between them due to the larger material contrast. We again emphasize that the velocity field carried by the rupture front is fault-parallel dominant.

The rupture propagation speed characteristics are shown in Figure 12. We observe that the mean and maximum  $V_r$  within both the sediment and the bedrock exceed the Eshelby speed. Both the mean and the maximum  $V_r$  in the sediment exceed local pressure wave speed  $C_p^l$ . That is not the case for the bedrock as shown in Figure 12b, which is similar to Figure 6b except for a delayed transition. The slip pulse propagation speeds  $V_H$  are estimated in Figure 12c-d to be  $\sim 2.85C_s^l$  within the sediment and  $\sim 1.6C_s^l$  within the bedrock. This apparent supersonic propagation is driven by the supershear rupture at depth and contributes to the complexity of the velocity field near the rupture tip.

Considering synthetic seismogram readings for Model B-2, we observe similar features to Model A-2, such as an initial large FP jump associated with the rupture tip passage, and then a second large FN jump associated with trailing Rayleigh. Within the FP component, we observe the influence of the multiple Mach cones which extend the large velocity pulse window prior to subsiding right before the trailing Rayleigh signature. The vertical component is also strongly amplified by the passage of the leading rupture tip.

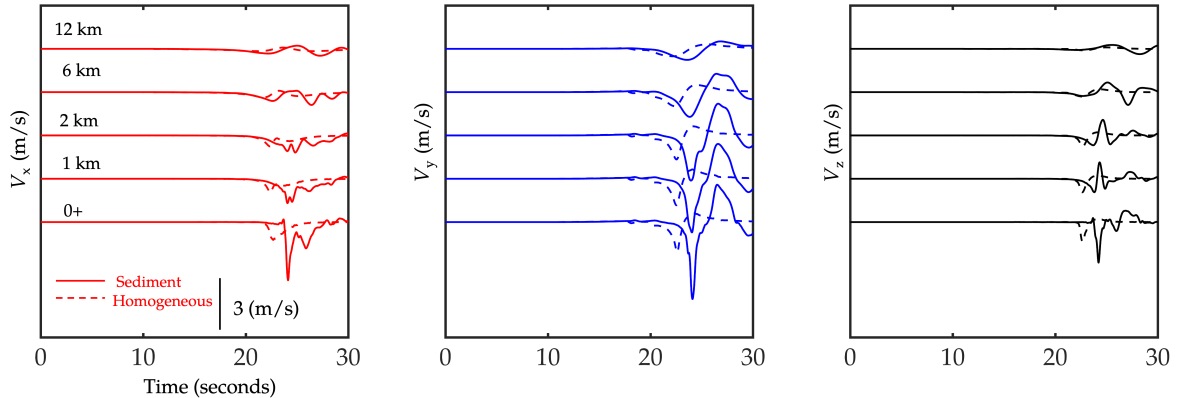


Figure 10: The role of sediment layer contrast in altering rupture ground motion characteristics for Model A-1 with  $S_o = 3.0$  and  $C_s^1 = 0.7C_s^2$ . (a) Fault-parallel (FP), (b) fault-perpendicular (FN) and (c) vertical velocity time histories at five different sites. Sites are located at 50 km along strike and at distances (0<sup>+</sup>, 1, 2, 6, 12) along the fault perpendicular direction.

### 3.3. Ground motion characteristics of subshear and supershear in the presence of sediments

In this section, we compare several key ground motion metrics for the following scenarios: (1) a subshear model  $S_o = 3$  with and without a sediment, and (2) a supershear model  $S_o = 1.3$ . We set up these choices so that on average the rupture propagation is almost identical between the homogeneous and sediment models. The first scenario corresponds to models A-1, and H-1 (see Table 1) we showed earlier. The second scenario corresponds to models A-3, and H-3 and has a rapid transition to supershear rupture speed.

In Figure 14, the orientation of peak ground velocity (PGV) is shown for the scenarios discussed earlier. In Figure 14A-B we observe that when the rupture is only propagating locally at supershear speeds, there is no difference in the orientation of PGV, as the amplification in the FP component is still not sufficient to exceed the FN component. This is consistent with our earlier observations that  $FN > FP$  does not necessarily exclude local supershear propagation. The distribution varies between the homogeneous model and the model with the sediment layer when the rupture is propagating globally at supershear speed as seen in Figure 14C-D. We observe that, in the model with the sediment layer, the FP component becomes dominant sooner. This is attributed to the role of the soft layer and rupture acceleration in amplifying the FP component and attenuating the FN one.

In Figure A.5 we explore the amplification factors for PGV by comparing the homogeneous model with the sediment model. We show the ratio between  $PGV_S$  and  $PGV_H$  for each component, where subscripts S and H indicate the sediment model and the homogeneous model respectively. We clearly see that the amplification of ground motion is heterogeneous within each individual component. In the fault-parallel direction, we observe that the PGV is amplified more near the fault at distances less than 5 km. This is explained by the nature of the local supersonic and supershear propagations amplifying the FP direction. Interestingly, we see that the FN component within the near-fault is not amplified but rather is decreased through the incorporation of sediment layers. However, this behavior is confined to near-fault locations. As discussed earlier, because the rupture characteristics themselves are influenced by the incorporation of the sediment layer, we see that the amplification between the different components is also not uniform, with the FP PGV amplification being different from the FN PGV amplification.

In Figure 15, we also examine the Fourier amplitude spectra (FAS) and spectral accelerations (PSa) for models with  $S_o = 3$ , at locations 1, 2, 5 km along the fault perpendicular direction, and 20, 30, 40, and 50 km along the strike. In general, as shown in Figure 15a,c,e,g, the model with the sediment layer (solid) has higher amplitudes than the homogeneous case (dashed). We also observe a higher frequency cut-off for models with the sediment layers in the near-fault region (1 and 2 km) versus their homogeneous counterparts. Within the spectral accelerations shown in Figure 15b,d,f,h, we observe generally larger peaks

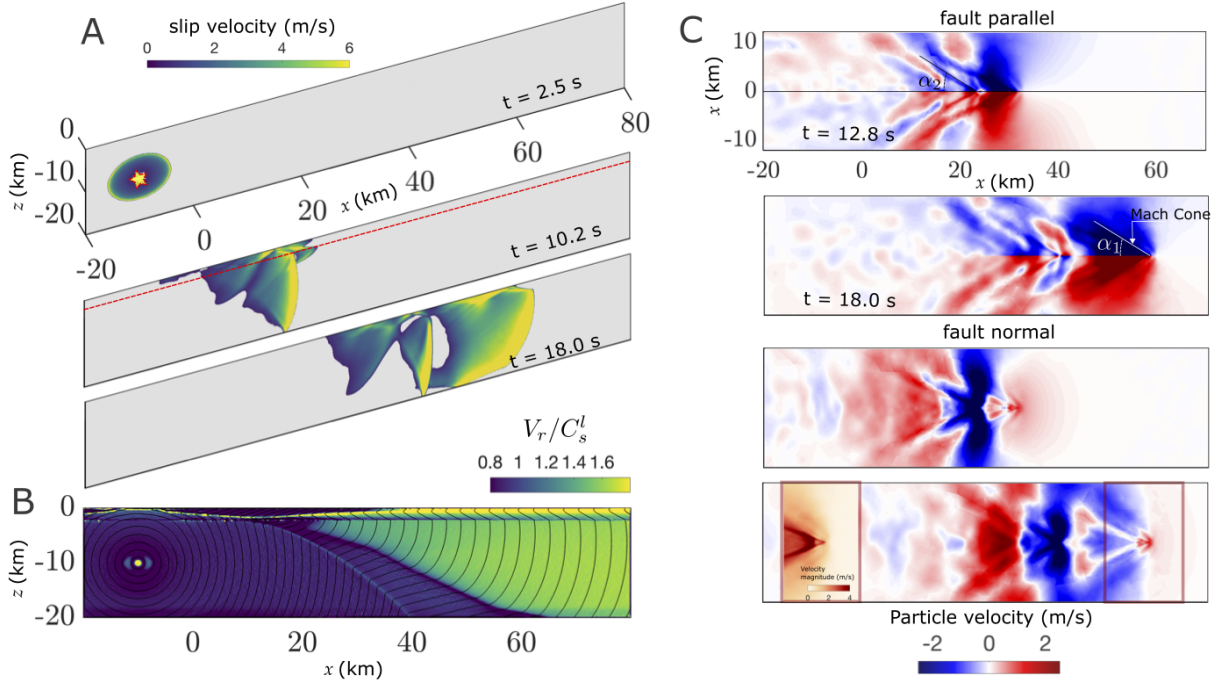


Figure 11: **The role of sediment layer contrast in altering rupture propagation and ground motion characteristics for Model B-2.** (a) snapshots of the rupture propagation at different times ( $t = 2.5$ ,  $10.2$ , and  $18.0$  s). (b) Contour of the normalized rupture speed  $V_r/C_s^l$ . (c) Contours of the fault-parallel and fault-normal particle velocity wave-field within near field of the fault at later stages of rupture propagation ( $t = 12.8$  s, and  $t = 18.0$  s). Zoomed figure in last panel shows the particle velocity magnitude near the rupture tip at  $t = 18.0$  s to highlight the structure of the Mach cone.

that shift toward smaller periods in the model with sediment layers. This observation is consistent with the higher cut-off frequency and is attributed to reflection within the shallow layer and local supershear effects. Furthermore, we observe that the decay of amplitude at higher frequency is larger for the sediment model compared to the homogeneous model. The differences in spectral accelerations between the homogeneous and sediment models highlight possible implications on the structural response of near-fault buildings and linear infrastructure that warrant further investigation.

Results for scenario 2 with  $S_o = 1.3$  are shown in Figure 16. First, we observe that the Fourier amplitude spectra (FAS) of both the homogeneous model and the sediment model are higher relative to scenario 1, which is consistent with the higher stress drop. We also observe that the decay of high-frequency content is different due to the nature of supershear attenuation. Similar to scenario 1, we observe that near-fault locations have a higher cut-off frequency before the decay of the FAS. Prior to supershear transition at  $x = 20$  km, both the sediment model and the homogeneous model have similar spectral acceleration peak locations; however, after transition, the first peak of the amplitude curve occurs at smaller periods.

Overall, we observe a clear distinction between the frequency content for local supershear propagation and global supershear propagation. The models with sediment have a higher cut-off frequency and the peaks of the spectral accelerations occur at smaller periods. These observations highlight the importance of considering the role of sediments on rupture propagation and consequently the ground motion characteristics.

#### 4. Discussion

In this work, we examine the role of sediment layers on the ground motion characteristics of both supershear and subshear ruptures. We compare the results of models with sediment layers and models with homogeneous media with the same initial  $S$  parameter. In our analysis, we have utilized a simple one-layer

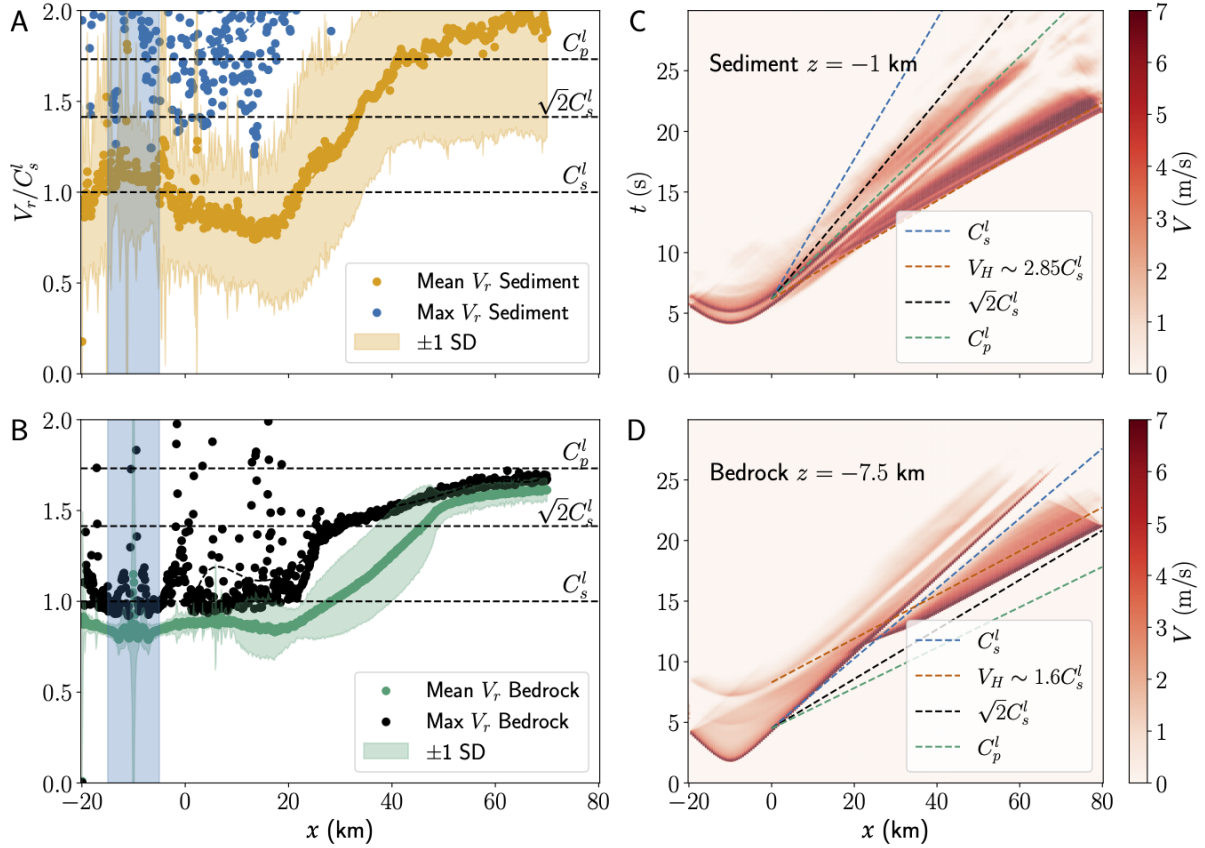


Figure 12: **The rupture propagation speeds in Model B-2** (a-b) Mean and maximum rupture propagation speed  $V_r$  within both the sediment and the bedrock. The shaded area represents the nucleation site of the rupture. (c-d) Spatiotemporal slip rate distribution at depth -1 km, and -7.5 km respectively to highlight local horizontal propagation speed  $V_H$  relative to local characteristics speeds  $C_s^l$ ,  $C_p^l$ , and  $\sqrt{2}C_s^l$ .

model with a sharp interface to isolate the effects of the sediment. This assumption is an over-simplification based on field studies which highlight that velocity structure continues to vary with depth. Accordingly, we also model a 1-D linear velocity structure that is obtained from the East Anatolian fault zone [64] as a representative case. The material properties of this velocity structure are tabulated in Table 2. We refer to these models as LVS-1 and LVS-2. In Figure A.3a we show the particle velocity field in the FP and FN direction for a case with initial  $S_o = 3$ . Similar to Model A-1, we observe the emergence of Mach cones at the free surface which are attributed to local supershear propagation. Further examining the synthetic seismograms and comparing with Model A-1, we observe almost identical features albeit with a small delay due to the different wave speed structure. We also explore differences in the limit that  $S_o = 1.6$ , and while differences do emerge, the same qualitative features are preserved with Model A-2.

We have also assumed in our model that the frictional properties ( $a$ , and  $b$ ) are uniformly velocity-weakening until 15 km depth. This assumption might also be inconsistent with some laboratory experiments on rock friction at low normal stress, which suggest a velocity-strengthening behavior [65, 66]. To account for this possibility, we further consider such variation in frictional properties by adding a velocity-strengthening patch near the free surface (coincident with low normal stress). In Figure A.4a-b we show Models A-1<sup>VS</sup> and A-2<sup>VS</sup> which are equivalent to Model A-1 and A-2 with the only difference being the depth-dependent ( $a - b$ ). The variation in ( $a - b$ ) is shown by the dashed line in Figure 1a. We note here that we retain the strong rate weakening behavior even when the friction is velocity-strengthening. We observe qualitative

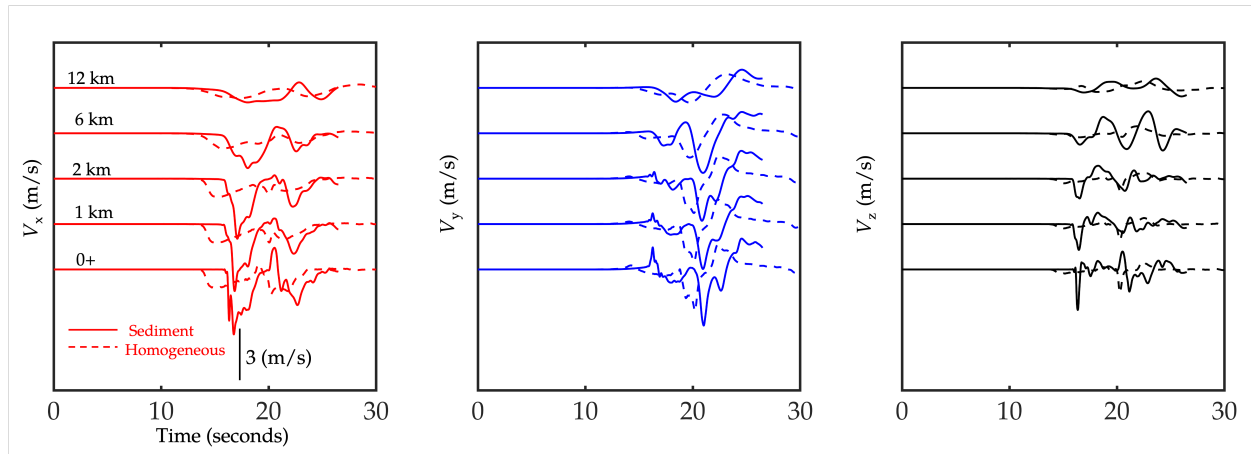


Figure 13: The role of sediment layer contrast in altering rupture ground motion characteristics for Model A-1 with  $\mathcal{S}_o = 3.0$  and  $C_s^1 = 0.7C_s^2$ . (a) Fault-parallel (FP), (b) fault-perpendicular (FN) and (c) vertical velocity time histories at five different sites. Sites are located at 50 km along strike and at distances (0<sup>+</sup>, 1, 2, 6, 12) along the fault perpendicular direction.

agreement between models with and without shallow VS layer, with features such as local supershear and supersonic propagation diminished but still preserved. Accordingly, we expect that there is a parameter space in which a VS layer could diminish the extent of observed local effects. Furthermore, we also emphasize that in addition to a shallow layer with different frictional parameters, it is expected that during frictional sliding this shallow portion of bulk would experience damage accumulation, due to low mean stress, in the form of inelastic deformations. Inelastic deformations could provide sufficient dissipation to inhibit some of the features we observe in our models.

Furthermore, to explore the role of sediment thickness, in Figure A.6 and Figure A.7 we represent the same models considered here with material contrast 70% and 50% but with sediment thickness of 5 km respectively. To distinguish the different models, we refer to the models with thicker sediment layers by the same model's name but with a subscript (\*). In the larger thickness models, we observe an increase in the extent of supershear propagation within the fault surface. By examining the synthetic ground motion records for Model B-1\*, we observe that despite rupture speed within the bedrock layer being subshear, the FP component of the near-fault (0<sup>+</sup>, 1 km) records is comparable to that of the FN component. This implies that at larger sediment thickness we can indeed recover the FP>FN condition observed in the global supershear case. We explain this behavior through the reduced influence of the subshear pulse on the free surface due to the increased depth of the sediment layer. Because of the altered rupture characteristics, we also observe that the amplitude of the FN leading pulse is smaller for Model B-1\* than Model A-1\* for near-fault stations (0<sup>+</sup>, 1, and 2 km), which is unexpected given the softer material.

Another effect of the thickness is shown in Figure A.7. We observe that all Models with  $\mathcal{S}_o = 1.6$  but one (Model B-2\*) transitions to global supershear. Model B-2\* features only local supershear propagation within the sediment layer while the rupture propagation speed within the bedrock remains subshear. In models A-2, B-2, we have shown that the presence of sediment promoted faster global supershear transition when compared to the homogeneous case, yet in Model B-2\* the sediment suppresses the transition entirely. This observation of non-monotonicity can be attributed to both a large thickness and large contrast greatly limiting the P-SV conversion that leads to free surface induced supershear at that choice of  $\mathcal{S}_o$ .

In the models that feature supershear propagation within the sediment layer only (i.e., shallow supershear), we find that the FN particle velocity jump is larger than the FP particle velocity jump. This observation *implies that FN>FP does not rule out shallow supershear propagation*. Furthermore, in all our models with sediment layers that feature global supershear propagation (saturating the seismogenic zone), we find that FP particle velocity jump is larger than the FN particle velocity jump. This observation *implies that FP>FN is a sufficient condition for identifying supershear propagation when considering this form of*

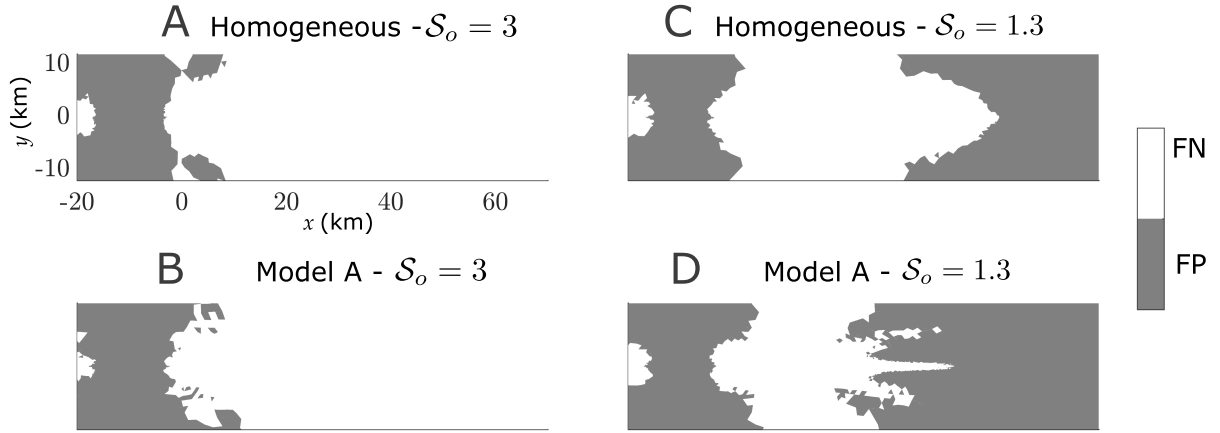


Figure 14: **Orientation of the PGV for different scenarios with local supershear and global supershear comparing homogeneous models and sediment models.** The maximum motion goes from predominantly fault-normal (white) to fault-parallel (grey).

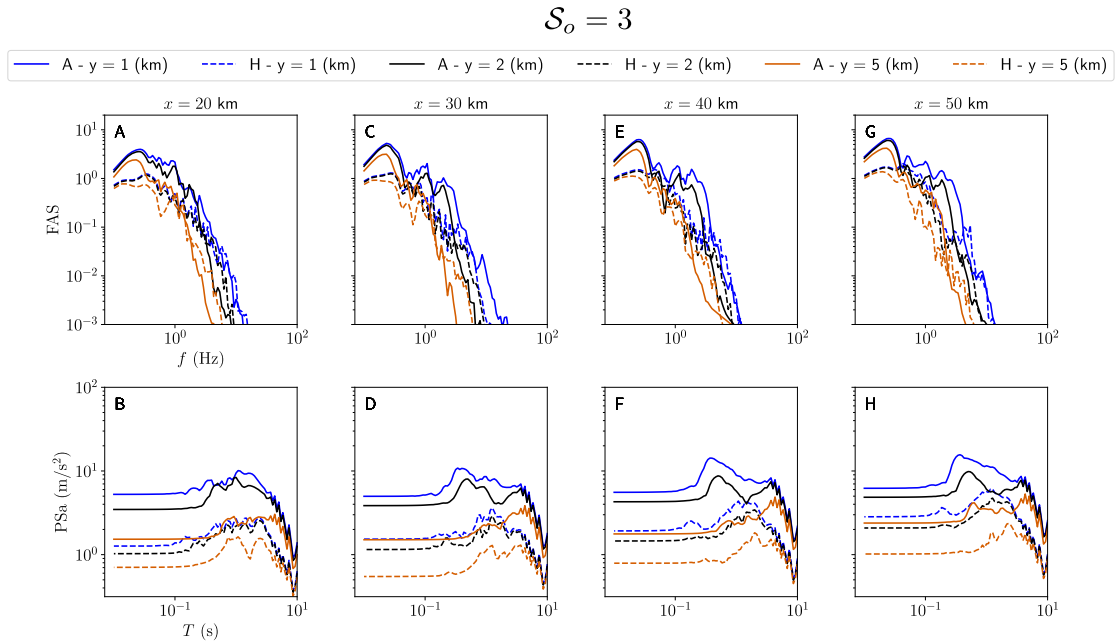


Figure 15: **Ground motion metrics comparison between models with sediment and homogeneous models.** (A) The Fourier amplitude spectra (FSA) and the spectral accelerations (PSa) for a homogeneous model (dashed lines) and sediment model (solid lines) with an initial  $S_o = 3$ . The site locations are 1, 2, 5 km along the fault perpendicular direction, and 20, 30, 40, and 50 km along the strike. The rupture propagation speed here is sub-shear for the homogeneous model and locally supershear for the sediment model.

*sedimentary structure.* It remains to be seen under what conditions, if any, such observation might vanish for global supershear.

It is important to highlight that our models are all linearly elastic. At large slip velocity, which are likely to be observed with strong rate weakening friction, it is probable that the surrounding bulk would start to accumulate inelastic deformation. The partitioning of deformations between bulk inelasticity and

$$S_o = 1.3$$

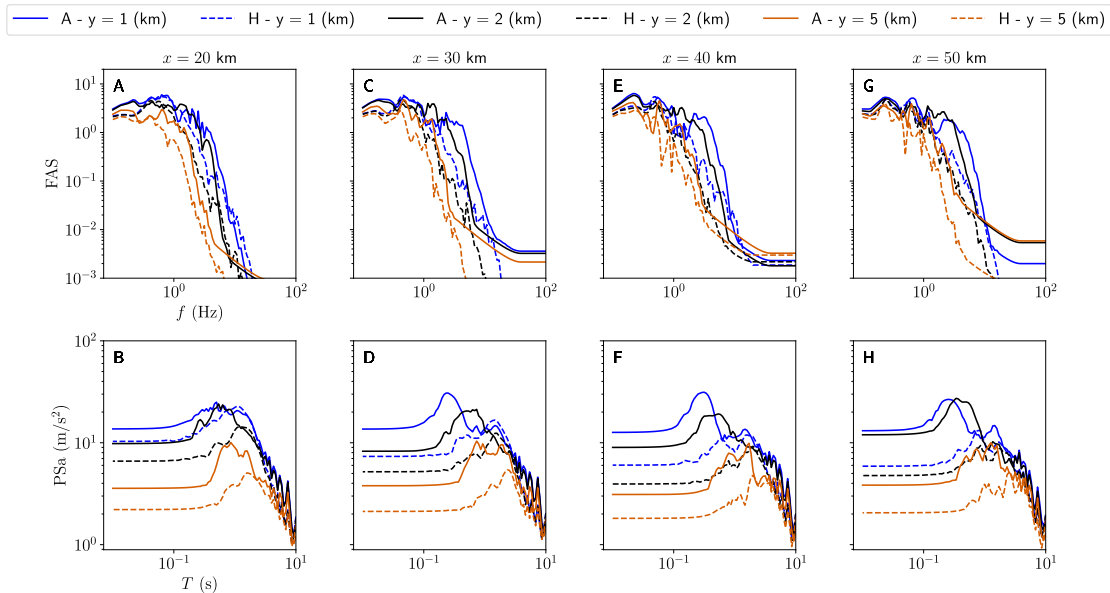


Figure 16: **Ground motion metrics comparison between models with sediment and homogeneous models.** The Fourier amplitude spectra (FSA) and the spectral accelerations (PSa) for a homogeneous model (dashed lines) and sediment model (solid lines) with an initial  $S_o = 1.3$ . The site locations are 1, 2, 5 km along the fault perpendicular direction, and 20, 30, 40, and 50 km along the strike. The rupture propagation speed here is globally supershear for both the homogeneous and the sediment model.

fault slip could potentially alter some of the observations in this study such as the propagation speed and the transition to supershear [67, 68, 69]. A potential future extension of this study would be to include Drucker-Prager like plasticity formulation [70, 51] or a continuum damage model [71, 72, 73] to study the implication of accumulating damage in sediment layers on the resultant ground motion characteristics.

Finally, we highlight that current methodologies of identifying earthquake rupture histories and consequently generating seismic hazard maps largely rely on kinematic inversion of the source properties. This is usually an ill-posed problem with large uncertainties due to source and path effects. This has been highlighted by the contradicting conclusions about the variability in rupture speed along the East Anatolian Fault in the recent Feb 6th 2023 Pazarcik Earthquake in Turkey, which happened to be well-instrumented. Theoretical models that can help constrain kinematic inversions are yet to mature to include realistic fault zone complexity. Now, with ever-increasing observational facilities, it is important to utilize realistic forward models to identify key characteristics of near-field ground motion records in the presence of realistic material heterogeneity to supplement inversion techniques and limit the degree of uncertainty. This will enable the scientific community to identify signatures within the ground motion records that will enable us to get rapid insights into the nature of the rupture propagation. These signatures can be utilized to constrain state-of-the-art kinematic inversion methods to better understand the rupture history. Such examples in which ground motion characteristics were used to identify rupture speeds already exist, such as in the cases of Denali and the Mw7.8 Turkey earthquakes [8, 6, 7].

## 5. Conclusions

Based on our study of ground motion characteristics of subshear and supershear ruptures in the presence of sediment layers, we draw the following conclusions:

1. The existence of a sediment layer with lower wave-speeds may lead to local supershear propagation

within the sediment while the propagation speed remains sub-shear in the bedrock. This results in the generation of Mach cones with a wide spectrum of angles based on the material contrast. This, in turn, enhances the ground shaking within the FP direction.

2. We find that the rupture propagation speed at the free surface (within the sediment) is coupled with the rupture propagation speed at depth, in models with sediment layers, despite the different material properties. This implies that it is possible to infer information about the rupture speed at depth based on surface measurements.
3. We find that  $FP > FN$  remains a sufficient condition to infer supershear propagation. However, we have found that supershear propagation in the shallow depth may be associated with  $FN > FP$ . Thus  $FN > FP$  may not rule out the possibility of local supershear propagation, but it remains indicative of dominant subshear propagation at depth.
4. We find that in models with the same rupture propagation speed (on average), the presence of sediment alters the ground motion characteristics significantly. In cases where the rupture is propagating globally at supershear speeds, we find that the sediment exclusively enhances the FP velocity pulse, while minimally changes the FN component. This leads to a PGV distribution that differs between the two models. We also find that sediment affects the frequency content of the ground motion, which would have implications on seismic hazard.
5. We observe, in all models with sediment layer, a substantial enhancement in the fault vertical component of the ground velocity which would have important implications on hazard including applications related to the seismic demand on linear infrastructure and the generation of tsunami waves.
6. We find that sediment layers influence the generation of supershear propagation within the bedrock. For models A-2, A-2\* and B-2 we find that sediment promotes global supershear. For model B-2\* which features a larger sediment thickness, we observe that the sediment hinders the supershear transition. This non-monotonic behavior highlights the importance of the sediment layer properties on free-surface-induced supershear transition.

These findings highlight the importance of considering heterogeneous subsurface material distribution in our physical models, as they may have significant implications on the source physics and the resulting ground motion characteristics. Our research provides new insights into the complex interactions between the sediment layers and the rupture dynamics. These findings are relevant for the continuous development of more robust seismic hazard assessments and for improving our understanding of earthquake processes in regions with sedimentary basins.

### Availability of data and materials

The software used to conduct the dynamic rupture model is open access and can be obtained at <https://github.com/wqseis/drdg3d>.

### Acknowledgement

M. A. would like to thank Eric Dunham for insightful discussion. The authors would also like to thank Grigorios Lavrentiadis for sharing the scripts used to characterize the ground motion. A.J.R. and M.A. acknowledges support by the Caltech/MCE Big Ideas Fund (BIF), as well as the Caltech Terrestrial Hazard Observation and Reporting Center (THOR). The simulations conducted in this study were possible thanks to the support of Amazon, through the AI4Science initiative. A. E. acknowledge support by the National Science Foundation CAREER award No. 1753249 for modeling complex fault zones. The authors acknowledge support from the Southern California Earthquake Center through a collaborative agreement between NSF. Grant Number: EAR0529922 and USGS. Grant Number: 07HQAG0008.

## Appendix

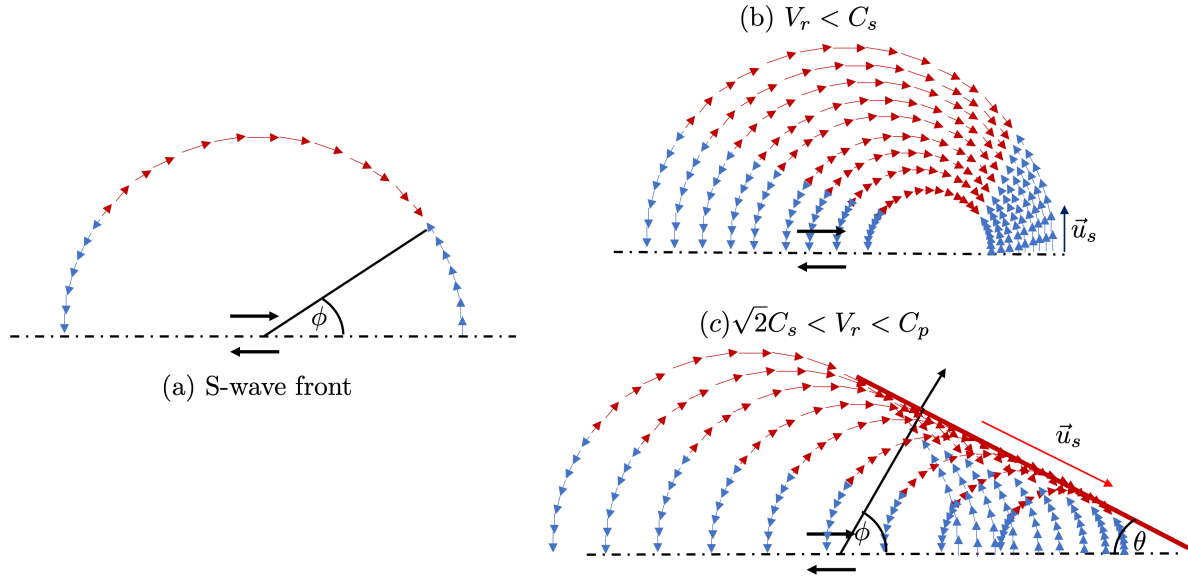


Figure A.1: Geometric characteristics of sub-shear and supershear (super-Eshelby) propagation.

Table 2: The 1D linear velocity model used in this study based on studies of the East Anatolian Fault (EAF) zone [64]

Depth (km)	$C_p$ (km/s)	$C_s$ (km/s)
0	3.88	2.04
1	4.52	2.43
2	5.62	3.03
4	5.75	3.31
6	5.85	3.38
8	5.96	3.43
10	6.00	3.44
12	6.05	3.46
16	6.32	3.62
20	6.40	3.67

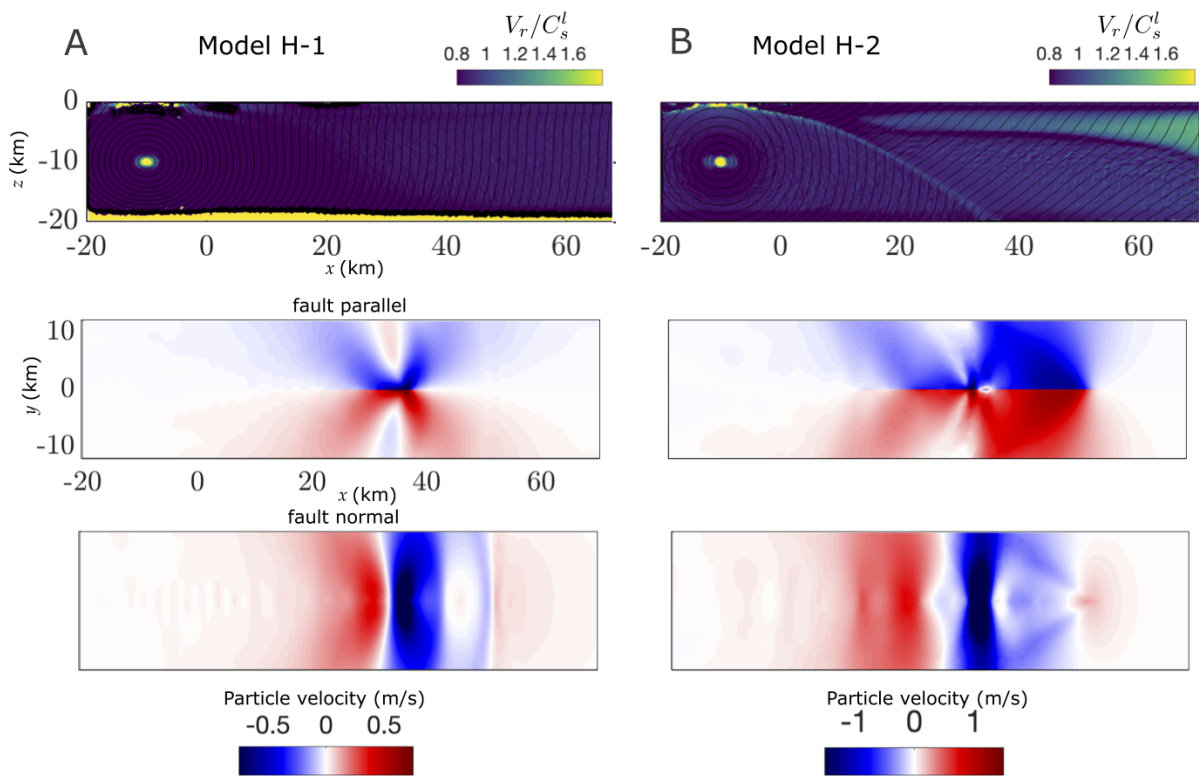


Figure A.2: **Reference homogeneous models H-1 and H-2.** (A) Model H-1 with  $S_o = 3$ . Top panel showing the normalized rupture propagation speed which is subshear. Bottom panel showing the signature subshear near-fault velocity wave-field. (B) Model H-2 with  $S_o = 1.6$ . Top panel showing the normalized rupture propagation speed and supershear transition. Bottom panel showing the Mach cone generation in the near-fault velocity wave-field.

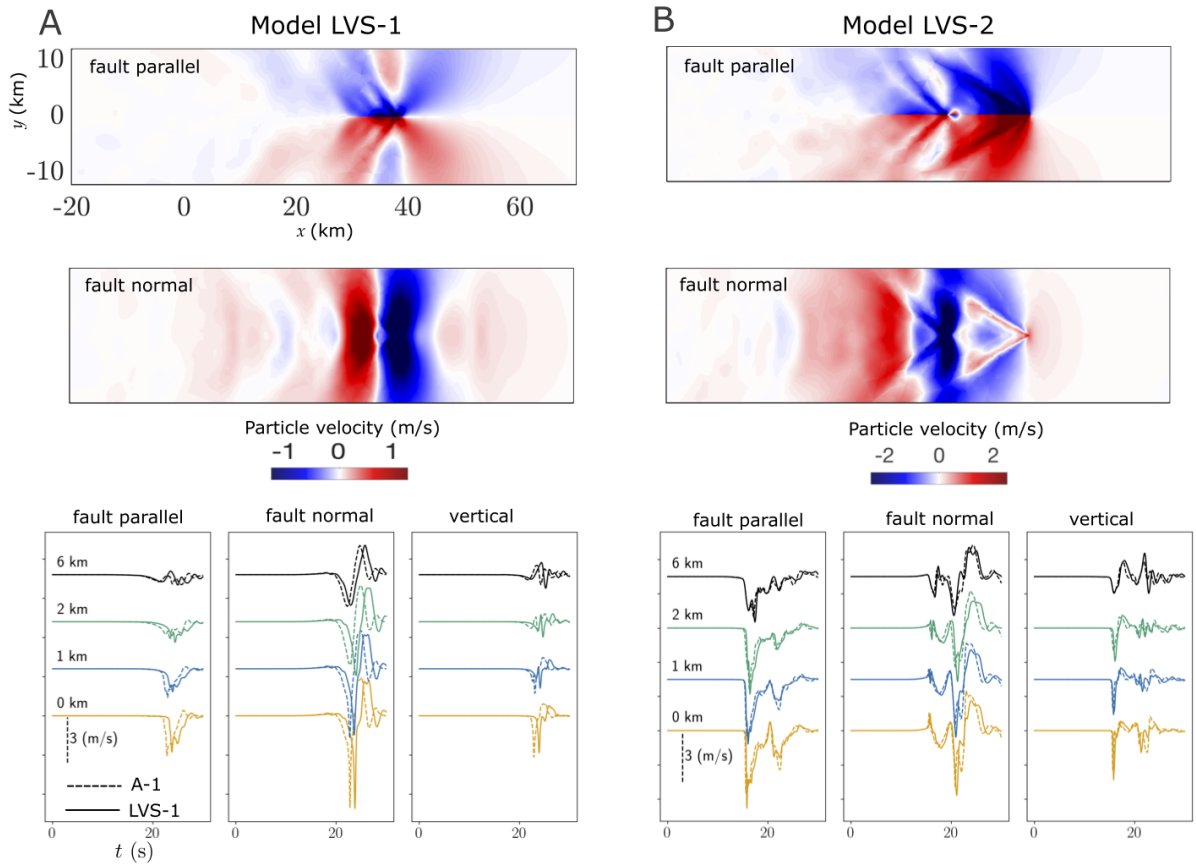


Figure A.3: **Models with linear velocity structure (LVS)**. (A-B) Model LVS-1 with  $S_o = 3$  and Model LVS-2 with  $S_o = 1.6$ . Top panel showing the the near-fault velocity wave-field which is very similar to model A-1. Bottom panel showing the Fault-parallel (FP), fault-perpendicular (FN) and vertical velocity time histories at four different sites. Sites are located at 50 km along strike and at distances ( $0^+$ , 1, 2, 6) km along the fault perpendicular direction. The ground motion is a slightly delayed version of model A-1 due to different wave-speeds.

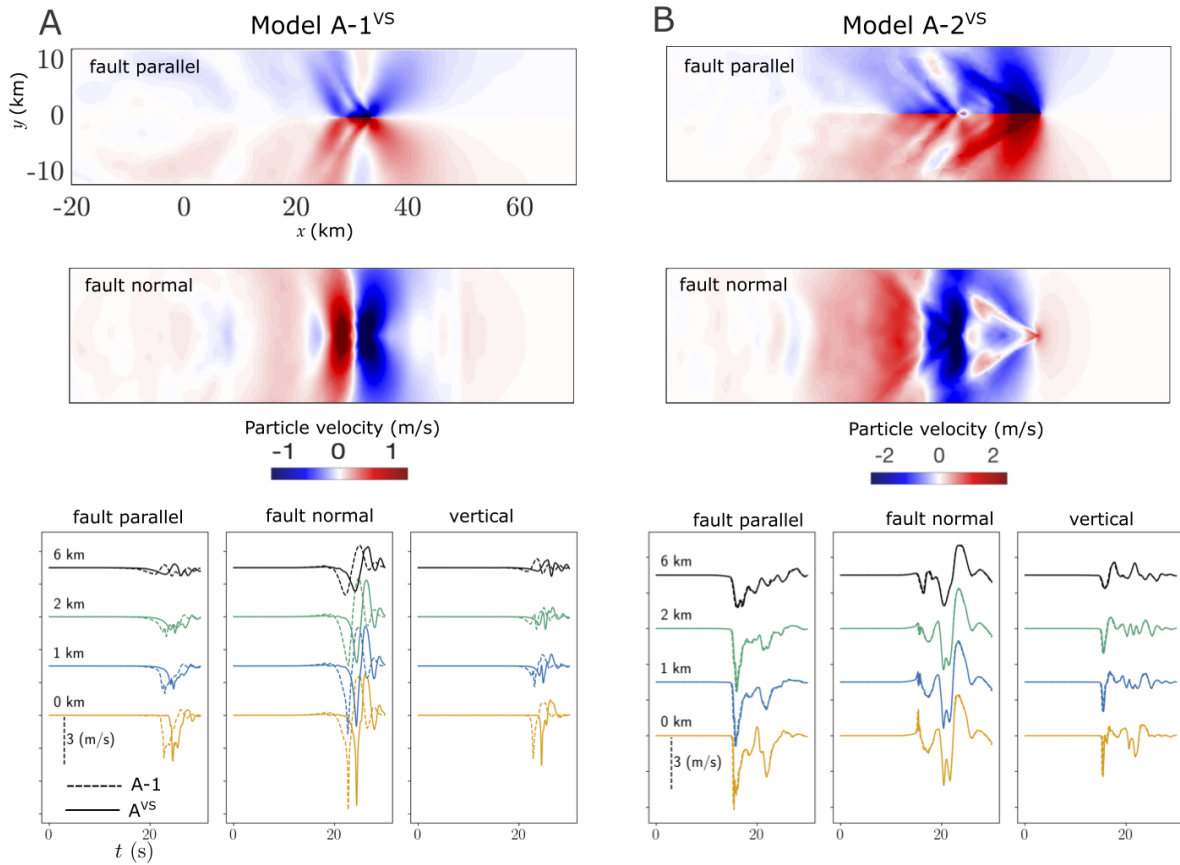


Figure A.4: **Models with a velocity-strengthening shallow layer.** (A-B) Model A-1<sup>VS</sup> with  $S_o = 3$  and Model A-2<sup>VS</sup> with  $S_o = 1.6$ . Top panel showing the the near-fault velocity wave-field which is very similar to model A-1. Bottom panel showing the Fault-parallel (FP), fault-perpendicular (FN) and vertical velocity time histories at four different sites. Sites are located at 50 km along strike and at distances ( $0^+$ , 1, 2, 6) km along the fault perpendicular direction. The ground motion is a slightly delayed version of model A-1 due to different wave-speeds. In order to have a velocity-strengthening behavior, the value of  $(a - b)$  increases linearly to 0.006 as we approach the free surface.

## PGV Amplification factor

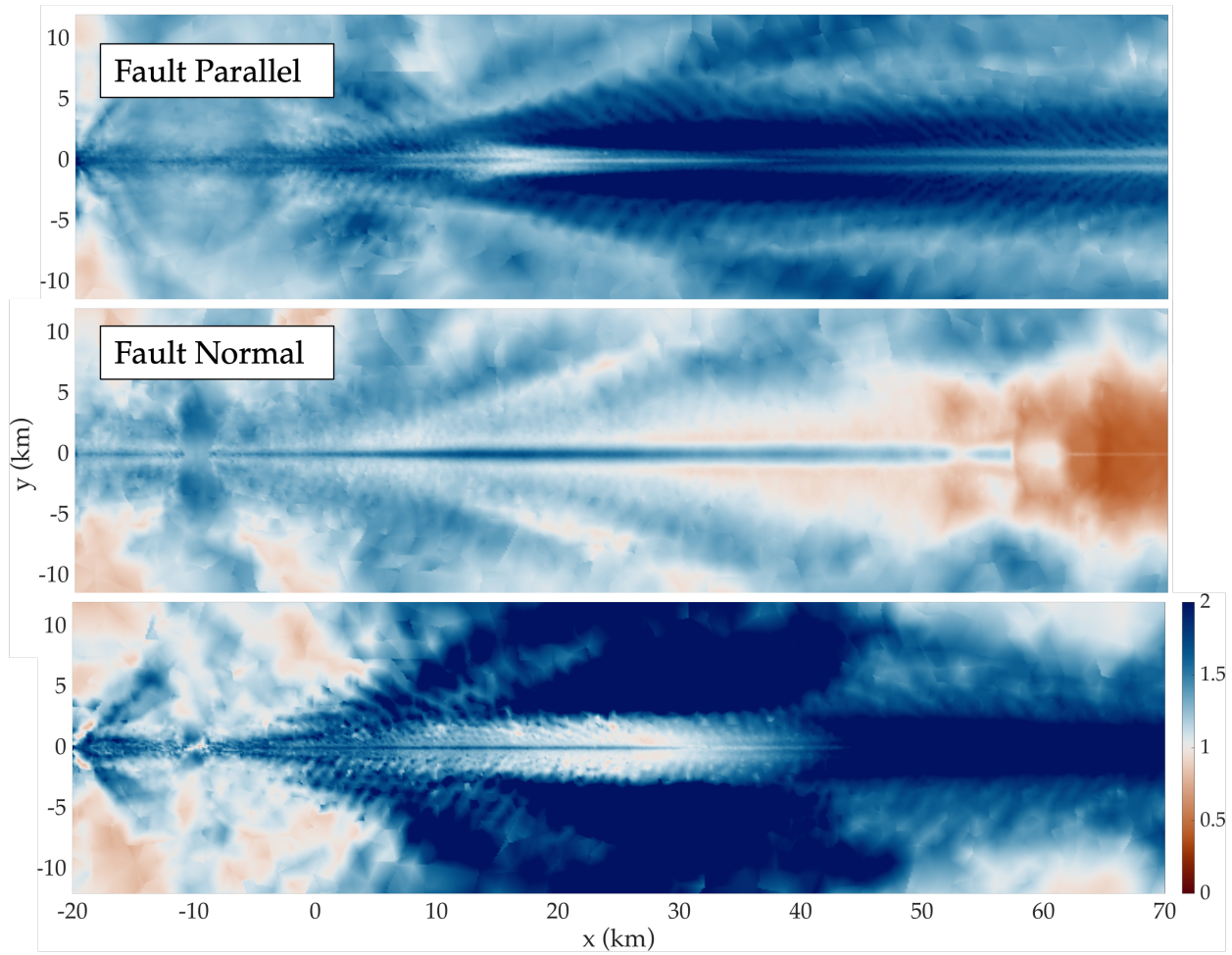


Figure A.5: The amplification and dampening of the PGV components (fault-parallel, fault-normal, and vertical). The contour colors show the ratio between the PGV of model A-3 and PGV model H-3.

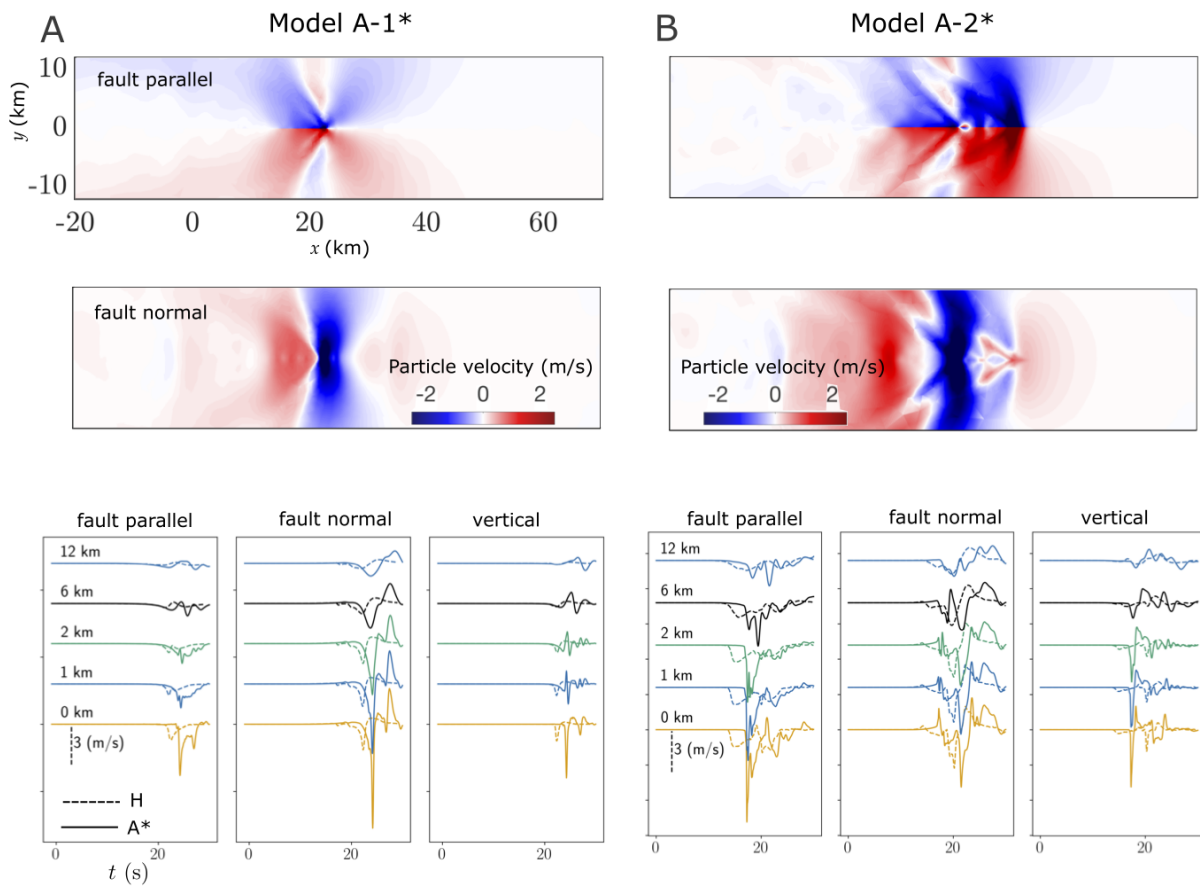


Figure A.6: **Models A (mild material contrast) with a 5 km thick sediment layer.** (A-B) Model A-1\* with  $S_0 = 3$  and Model A-2\* with  $S_0 = 1.6$ . Top panel showing the the near-fault velocity wave-field which is very similar to model A-1. Bottom panel showing the Fault-parallel (FP), fault-perpendicular (FN) and vertical velocity time histories at four different sites. Sites are located at 50 km along strike and at distances (0<sup>+</sup>, 1, 2, 6, 12) km along the fault perpendicular direction.

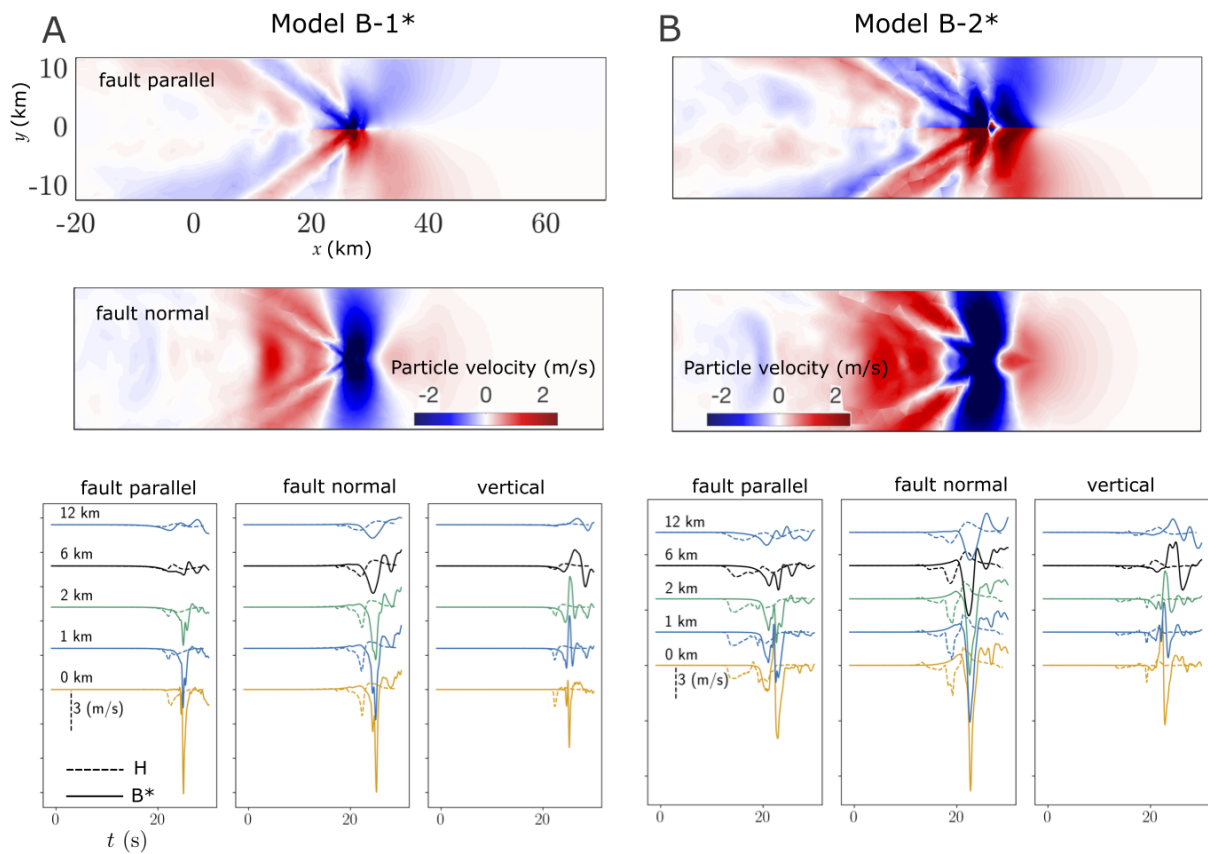


Figure A.7: **Models B (strong material contrast) with a 5 km thick sediment layer.** (A-B) Model B-1\* with  $S_o = 3$  and Model B-2\* with  $S_o = 1.6$ . Top panel showing the the near-fault velocity wave-field which is very similar to model A-1. Bottom panel showing the Fault-parallel (FP), fault-perpendicular (FN) and vertical velocity time histories at four different sites. Sites are located at 50 km along strike and at distances (0<sup>+</sup>, 1, 2, 6, 12) km along the fault perpendicular direction.

## References

- [1] Eric M Dunham and Ralph J Archuleta. Evidence for a supershear transient during the 2002 denali fault earthquake. *Bulletin of the Seismological Society of America*, 94(6B):S256–S268, 2004.
- [2] Kristoffer T Walker and Peter M Shearer. Illuminating the near-sonic rupture velocities of the intracontinental kokoxili mw 7.8 and denali fault mw 7.9 strike-slip earthquakes with global p wave back projection imaging. *Journal of Geophysical Research: Solid Earth*, 114(B2), 2009.
- [3] Hideo Aochi, Virginie Durand, and John Douglas. Influence of super-shear earthquake rupture models on simulated near-source ground motion from the 1999 izmit, turkey, earthquake. *Bulletin of the Seismological Society of America*, 101(2):726–741, 2011.
- [4] M Mello, HS Bhat, AJ Rosakis, and H Kanamori. Reproducing the supershear portion of the 2002 denali earthquake rupture in laboratory. *Earth and Planetary Science Letters*, 387:89–96, 2014.
- [5] Yoshihiro Kaneko and Hiroyuki Goto. The origin of large, long-period near-fault ground velocities during surface-breaking strike-slip earthquakes. *Geophysical Research Letters*, 49(10):e2022GL098029, 2022.
- [6] Ares Rosakis, Mohamed Abdelmeguid, and Ahmed Elbanna. Evidence of early supershear transition in the mw 7.8 kahramanmaraş earthquake from near-field records. *arXiv preprint arXiv:2302.07214*, 2023.
- [7] Mohamed Abdelmeguid, Chunhui Zhao, Esref Yalcinkaya, George Gazetas, Ahmed Elbanna, and Ares Rosakis. Dynamics of episodic supershear in the 2023 m7. 8 kahramanmaraş/pazarçik earthquake, revealed by near-field records and computational modeling. *Communications Earth & Environment*, 4(1):456, 2023.
- [8] Eric M. Dunham and Ralph J. Archuleta. Evidence for a supershear transient during the 2002 Denali fault earthquake. *Bulletin of the Seismological Society of America*, 94(6 SUPPL. B):256–268, 2004.
- [9] WL Ellsworth, M Celebi, JR Evans, EG Jensen, R Kayen, MC Metz, DJ Nyman, JW Roddick, P Spudich, and CD Stephens. Near-field ground motion of the 2002 denali fault, alaska, earthquake recorded at pump station 10. *Earthquake spectra*, 20(3):597–615, 2004.
- [10] M. Mello, H. S. Bhat, A. J. Rosakis, and H. Kanamori. Reproducing the supershear portion of the 2002 Denali earthquake rupture in laboratory. *Earth and Planetary Science Letters*, 387:89–96, 2014.
- [11] Kaiwen Xia, Ares J Rosakis, and Hiroo Kanamori. Laboratory earthquakes: The sub-rayleigh-to-supershear rupture transition. *Science*, 303(5665):1859–1861, 2004.
- [12] Kaiwen Xia, Ares J Rosakis, Hiroo Kanamori, and James R Rice. Laboratory earthquakes along inhomogeneous faults: Directionality and supershear. *Science*, 308(5722):681–684, 2005.
- [13] Michael Mello, HS Bhat, AJ Rosakis, and H Kanamori. Identifying the unique ground motion signatures of supershear earthquakes: Theory and experiments. *Tectonophysics*, 493(3-4):297–326, 2010.
- [14] Michael Mello, Harsha S. Bhat, and Ares J. Rosakis. Spatiotemporal properties of Sub-Rayleigh and supershear rupture velocity fields: Theory and experiments. *Journal of the Mechanics and Physics of Solids*, 93:153–181, 8 2016.
- [15] Xiao Lu, Ares J. Rosakis, and Nadia Lapusta. Rupture modes in laboratory earthquakes: Effect of fault prestress and nucleation conditions. *Journal of Geophysical Research: Solid Earth*, 115(12):1–25, 2010.
- [16] V. Rubino, A. J. Rosakis, and N. Lapusta. Understanding dynamic friction through spontaneously evolving laboratory earthquakes. *Nature Communications*, 8(May):1–12, 2017.
- [17] Michel Bouchon, Marie-Paule Bouin, Hayrullah Karabulut, M. Nafi Toksöz, Michel Dietrich, and Ares J. Rosakis. How fast is rupture during an earthquake? New insights from the 1999 Turkey Earthquakes. *Geophysical Research Letters*, 28(14):2723–2726, 7 2001.
- [18] Hongyu Zeng, Shengji Wei, and Ares Rosakis. A travel-time path calibration strategy for back-projection of large earthquakes and its application and validation through the segmented super-shear rupture imaging of the 2002 mw 7.9 denali earthquake. *Journal of Geophysical Research: Solid Earth*, 127(6):e2022JB024359, 2022.
- [19] V. Rubino, A. J. Rosakis, and N. Lapusta. Spatiotemporal Properties of Sub-Rayleigh and Supershear Ruptures Inferred From Full-Field Dynamic Imaging of Laboratory Experiments. *Journal of Geophysical Research: Solid Earth*, 125(2):1–25, 2020.
- [20] Eric M Dunham and Ralph J Archuleta. Near-source ground motion from steady state dynamic rupture pulses. *Geophysical Research Letters*, 32(3), 2005.
- [21] Han Bao, Jean-Paul Ampuero, Lingsen Meng, Eric J Fielding, Cunren Liang, Christopher WD Milliner, Tian Feng, and Hui Huang. Early and persistent supershear rupture of the 2018 magnitude 7.5 palu earthquake. *Nature Geoscience*, 12(3):200–205, 2019.
- [22] Han Bao, Liuwei Xu, Lingsen Meng, Jean-Paul Ampuero, Lei Gao, and Haijiang Zhang. Global frequency of oceanic and continental supershear earthquakes. *Nature Geoscience*, 15(11):942–949, 2022.
- [23] Seok Goo Song, Gregory C Beroza, and Paul Segall. A unified source model for the 1906 san francisco earthquake. *Bulletin of the Seismological Society of America*, 98(2):823–831, 2008.
- [24] Y. Kaneko and N. Lapusta. Supershear transition due to a free surface in 3-D simulations of spontaneous dynamic rupture on vertical strike-slip faults. *Tectonophysics*, 493(3-4):272–284, 2010.
- [25] Feng Hu, David D. Oglesby, and Xiaofei Chen. The Sustainability of Free-Surface-Induced Supershear Rupture on Strike-Slip Faults. *Geophysical Research Letters*, 46(16):9537–9543, 2019.
- [26] Feng Hu, David D Oglesby, and Xiaofei Chen. The effect of depth-dependent stress in controlling free-surface-induced supershear rupture on strike-slip faults. *Journal of Geophysical Research: Solid Earth*, 126(5):e2020JB021459, 2021.
- [27] Jiankuan Xu, Xiaofei Chen, Peng Liu, and Zhenguo Zhang. Ground motion signatures of supershear ruptures in the burridge-andrews and free-surface-induced mechanisms. *Tectonophysics*, 791:228570, 2020.

- [28] Gabriele Albertini and David S Kammer. Off-fault heterogeneities promote supershear transition of dynamic mode ii cracks. *Journal of Geophysical Research: Solid Earth*, 122(8):6625–6641, 2017.
- [29] Xiao Ma and AE Elbanna. Effect of off-fault low-velocity elastic inclusions on supershear rupture dynamics. *Geophysical Journal International*, 203(1):664–677, 2015.
- [30] H Shlomai, M Adda-Bedia, RE Arias, and Jay Fineberg. Supershear frictional ruptures along bimaterial interfaces. *Journal of Geophysical Research: Solid Earth*, 125(8):e2020JB019829, 2020.
- [31] Yihe Huang and Jean-Paul Ampuero. Pulse-like ruptures induced by low-velocity fault zones. *Journal of Geophysical Research: Solid Earth*, 116(B12), 2011.
- [32] Yihe Huang, Jean-Paul Ampuero, and Don V Helmberger. The potential for supershear earthquakes in damaged fault zones—theory and observations. *Earth and Planetary Science Letters*, 433:109–115, 2016.
- [33] Benchun Duan. Effects of low-velocity fault zones on dynamic ruptures with nonelastic off-fault response. *Geophysical Research Letters*, 35(4), 2008.
- [34] Jagdish Chandra Vyas, Paul Martin Mai, Martin Galis, Eric M Dunham, and Walter Imperatori. Mach wave properties in the presence of source and medium heterogeneity. *Geophysical Journal International*, 214(3):2035–2052, 2018.
- [35] Jiankuan Xu, Zhenguo Zhang, and Xiaofei Chen. The effects of sediments on supershear rupture. *Tectonophysics*, 805:228777, 2021.
- [36] Nicholas Christie-Blick and Kevin T Biddle. Deformation and basin formation along strike-slip faults. 1985.
- [37] Tor H Nilsen. Strike-slip basins. *Tectonics of sedimentary basins*, pages 423–457, 1995.
- [38] Raymond V Ingersoll. Tectonics of sedimentary basins. *Geological Society of America Bulletin*, 100(11):1704–1719, 1988.
- [39] Steven M Day, Robert Graves, Jacobo Bielak, Douglas Dreger, Shawn Larsen, Kim B Olsen, Arben Pitarka, and Leonardo Ramirez-Guzman. Model for basin effects on long-period response spectra in southern california. *Earthquake Spectra*, 24(1):257–277, 2008.
- [40] Arthur Frankel, William Stephenson, and David Carver. Sedimentary basin effects in seattle, washington: Ground-motion observations and 3d simulations. *Bulletin of the Seismological Society of America*, 99(3):1579–1611, 2009.
- [41] James H Dieterich. Modeling of rock friction: 1. experimental results and constitutive equations. *Journal of Geophysical Research: Solid Earth*, 84(B5):2161–2168, 1979.
- [42] Andy Ruina. Slip instability and state variable friction laws. *Journal of Geophysical Research: Solid Earth*, 88(B12):10359–10370, 1983.
- [43] James R Rice and Simon T Tse. Dynamic motion of a single degree of freedom system following a rate and state dependent friction law. *Journal of Geophysical Research: Solid Earth*, 91(B1):521–530, 1986.
- [44] V Rubino, AJ Rosakis, and N Lapusta. Understanding dynamic friction through spontaneously evolving laboratory earthquakes. *Nature communications*, 8(1):15991, 2017.
- [45] Vito Rubino, Yuval Tal, Ares J Rosakis, and Nadia Lapusta. Evolution of dynamic shear strength of frictional interfaces during rapid normal stress variations. In *EPJ Web of Conferences*, volume 250, page 01016. EDP Sciences, 2021.
- [46] V Rubino, N Lapusta, and AJ Rosakis. Intermittent lab earthquakes in dynamically weakening fault gouge. *Nature*, 606(7916):922–929, 2022.
- [47] Yuval Tal, Vito Rubino, Ares J Rosakis, and Nadia Lapusta. Illuminating the physics of dynamic friction through laboratory earthquakes on thrust faults. *Proceedings of the National Academy of Sciences*, 117(35):21095–21100, 2020.
- [48] NM Beeler, TE Tullis, and DL Goldsby. Constitutive relationships and physical basis of fault strength due to flash heating. *Journal of Geophysical Research: Solid Earth*, 113(B1), 2008.
- [49] Akito Tsutsumi and Toshihiko Shimamoto. High-velocity frictional properties of gabbro. *Geophysical Research Letters*, 24(6):699–702, 1997.
- [50] Takehiro Hirose and Toshihiko Shimamoto. Growth of molten zone as a mechanism of slip weakening of simulated faults in gabbro during frictional melting. *Journal of Geophysical Research: Solid Earth*, 110(B5), 2005.
- [51] Eric M. Dunham, David Belanger, Lin Cong, and Jeremy E. Kozdon. Earthquake ruptures with strongly rate-weakening friction and off-fault plasticity, part 1: Planar faults. *Bulletin of the Seismological Society of America*, 101(5):2296–2307, 2011.
- [52] DJ Andrews. Rupture velocity of plane strain shear cracks. *Journal of Geophysical Research*, 81(32):5679–5687, 1976.
- [53] Shamita Das and Keiiti Aki. A numerical study of two-dimensional spontaneous rupture propagation. *Geophysical journal international*, 50(3):643–668, 1977.
- [54] Eric M Dunham. Conditions governing the occurrence of supershear ruptures under slip-weakening friction. *Journal of Geophysical Research: Solid Earth*, 112(B7), 2007.
- [55] Ares J Rosakis, Kaiwen Xia, G Lykotraftis, and Hiroo Kanamori. Dynamic shear rupture in frictional interfaces: Speeds, directionality, and modes. *Earthquake Seismology*, 4:153–192, 2007.
- [56] Y Kaneko and N Lapusta. Supershear transition due to a free surface in 3-d simulations of spontaneous dynamic rupture on vertical strike-slip faults. *Tectonophysics*, 493(3-4):272–284, 2010.
- [57] Wenqiang Zhang, Yajing Liu, and Xiaofei Chen. A mixed-flux-based nodal discontinuous galerkin method for 3d dynamic rupture modeling. *Journal of Geophysical Research: Solid Earth*, page e2022JB025817, 2023.
- [58] Sezim Ezgi Güvercin, Hayrullah Karabulut, A Özgün Konca, Uğur Doğan, and Semih Ergintav. Active seismotectonics of the east anatolian fault. *Geophysical Journal International*, 230(1):50–69, 2022.
- [59] Robert Burridge. Admissible speeds for plane-strain self-similar shear cracks with friction but lacking cohesion. *Geophysical Journal International*, 35(4):439–455, 1973.
- [60] Harsha S Bhat, Renata Dmowska, James R Rice, and Nobuki Kame. Dynamic slip transfer from the denali to totsunda faults, alaska: Testing theory for fault branching. *Bulletin of the Seismological Society of America*, 94(6B):S202–S213, 2004.

- [61] Huihui Weng and Jean-Paul Ampuero. Continuum of earthquake rupture speeds enabled by oblique slip. *Nature Geoscience*, 13(12):817–821, 2020.
- [62] Keiiti Aki and Paul G Richards. *Quantitative seismology*. 2002.
- [63] Eric Michael Dunham. The dynamics and near-source ground motion of supershear earthquakes. 2005.
- [64] Sezim Ezgi Güvercin, Hayrullah Karabulut, A. Özgün Konca, Uğur Doğan, and Semih Ergintav. Active seismotectonics of the East Anatolian Fault. *Geophysical Journal International*, 230(1):50–69, 7 2022.
- [65] Chris J Marone, CH Scholtz, and Roger Bilham. On the mechanics of earthquake afterslip. *Journal of Geophysical Research: Solid Earth*, 96(B5):8441–8452, 1991.
- [66] Chris Marone. Laboratory-derived friction laws and their application to seismic faulting. *Annual Review of Earth and Planetary Sciences*, 26(1):643–696, 1998.
- [67] Simon Preuss, Jean Paul Ampuero, Taras Gerya, and Ylona van Dinther. Characteristics of earthquake ruptures and dynamic off-fault deformation on propagating faults. *Solid Earth Discussions*, 2020:1–39, 2020.
- [68] Mohamed Abdelmeguid, Md Shumon Mia, and Ahmed Elbanna. On the interplay between distributed bulk plasticity and local fault slip in evolving fault zone complexity. 2024.
- [69] Yehuda Ben-Zion and Zheqiang Shi. Dynamic rupture on a material interface with spontaneous generation of plastic strain in the bulk. *Earth and Planetary Science Letters*, 236(1-2):486–496, 2005.
- [70] Mohamed Abdelmeguid and Ahmed Elbanna. Modeling sequences of earthquakes and aseismic slip (seas) in elasto-plastic fault zones with a hybrid finite element spectral boundary integral scheme. *Journal of Geophysical Research: Solid Earth*, 127(12):e2022JB024548, 2022.
- [71] Vladimir Lyakhovskiy and Yehuda Ben-Zion. Damage–breakage rheology model and solid–granular transition near brittle instability. *Journal of the Mechanics and Physics of Solids*, 64:184–197, 2014.
- [72] Vladimir Lyakhovskiy, Yehuda Ben-Zion, Assen Ilchev, and Aleksander Mendecki. Dynamic rupture in a damage-breakage rheology model. *Geophysical Journal International*, 206(2):1126–1143, 2016.
- [73] Chunhui Zhao, Md Shumon Mia, Ahmed Elbanna, and Ben-Zion Yehuda. Dynamic rupture modeling in a complex fault zone with distributed and localized damage. *preprint*, 2024.